



Calhoun: The NPS Institutional Archive
DSpace Repository

Theses and Dissertations

1. Thesis and Dissertation Collection, all items

2005-09

Higher-order modes in free electron lasers

Williams, Brett W.

Monterey, California. Naval Postgraduate School

<http://hdl.handle.net/10945/1979>

This publication is a work of the U.S. Government as defined in Title 17, United States Code, Section 101. Copyright protection is not available for this work in the United States.

Downloaded from NPS Archive: Calhoun



Calhoun is the Naval Postgraduate School's public access digital repository for research materials and institutional publications created by the NPS community. Calhoun is named for Professor of Mathematics Guy K. Calhoun, NPS's first appointed -- and published -- scholarly author.

Dudley Knox Library / Naval Postgraduate School
411 Dyer Road / 1 University Circle
Monterey, California USA 93943

<http://www.nps.edu/library>



NAVAL
POSTGRADUATE
SCHOOL

MONTEREY, CALIFORNIA

THESIS

HIGHER-ORDER MODES
IN FREE ELECTRON LASERS

by

B. W. Williams

September 2005

Thesis Advisor:	W. B. Colson
Second Reader:	R. Armstead

Approved for public release; distribution is unlimited.

THIS PAGE INTENTIONALLY LEFT BLANK

REPORT DOCUMENTATION PAGE			<i>Form Approved OMB No. 0704-0188</i>	
Public reporting burden for this collection of information is estimated to average 1 hour per response, including the time for reviewing instruction, searching existing data sources, gathering and maintaining the data needed, and completing and reviewing the collection of information. Send comments regarding this burden estimate or any other aspect of this collection of information, including suggestions for reducing this burden, to Washington headquarters Services, Directorate for Information Operations and Reports, 1215 Jefferson Davis Highway, Suite 1204, Arlington, VA 22202-4302, and to the Office of Management and Budget, Paperwork Reduction Project (0704-0188) Washington DC 20503.				
1. AGENCY USE ONLY (Leave blank)		2. REPORT DATE September 2005	3. REPORT TYPE AND DATES COVERED Master's Thesis	
4. TITLE AND SUBTITLE: Higher-Order Modes in Free Electron Lasers			5. FUNDING NUMBERS	
6. AUTHOR(S) B. W. Williams				
7. PERFORMING ORGANIZATION NAME(S) AND ADDRESS(ES) Naval Postgraduate School Monterey, CA 93943-5000			8. PERFORMING ORGANIZATION REPORT NUMBER	
9. SPONSORING / MONITORING AGENCY NAME(S) AND ADDRESS(ES) N/A			10. SPONSORING / MONITORING AGENCY REPORT NUMBER	
11. SUPPLEMENTARY NOTES The views expressed in this thesis are those of the author and do not reflect the official policy or position of the Department of Defense or the U.S. Government.				
12a. DISTRIBUTION / AVAILABILITY STATEMENT Approved for public release - distribution is unlimited.			12b. DISTRIBUTION CODE	
13. ABSTRACT (maximum 200 words) Free electron laser theory is developed from the Maxwell and Lorentz force equations; the properties and characteristics of the laser are reviewed. The wave equation is solved for the fundamental Gaussian mode, and higher-order modes in Cartesian and cylindrical coordinate spaces, yielding expressions for the complete and orthogonal basis sets of Hermite- and Laguerre-Gaussian beams. Motivated by the evident inclusion of higher-order modes in free electron laser simulations, a tool is developed for the higher-order (in particular Laguerre-Gaussian) modal analysis of simulated free electron laser beams.				
14. SUBJECT TERMS Free electron lasers, higher-order modes, Laguerre-Gaussian laser beams			15. NUMBER OF PAGES 75	
			16. PRICE CODE	
17. SECURITY CLASSIFICATION OF REPORT Unclassified	18. SECURITY CLASSIFICATION OF THIS PAGE Unclassified	19. SECURITY CLASSIFICATION OF ABSTRACT Unclassified	20. LIMITATION OF ABSTRACT UL	

THIS PAGE INTENTIONALLY LEFT BLANK

Approved for public release - distribution is unlimited.

HIGHER-ORDER MODES IN FREE ELECTRON LASERS

Brett W. Williams
Lieutenant, United States Navy
B.A. Chemistry, State University of New York at Stony Brook, 1998

Submitted in partial fulfillment of the
requirements for the degree of

MASTER OF SCIENCE IN PHYSICS

from the

**NAVAL POSTGRADUATE SCHOOL
September 2005**

Author: Brett W. Williams

Approved by: William B. Colson
Thesis Advisor

Robert L. Armstead
Second Reader

James H. Luscombe
Chairman, Department of Physics

THIS PAGE INTENTIONALLY LEFT BLANK

ABSTRACT

Free electron laser theory is developed from the Maxwell and Lorentz force equations; the properties and characteristics of the laser are reviewed. The wave equation is solved for the fundamental Gaussian mode, and higher-order modes in Cartesian and cylindrical coordinate spaces, yielding expressions for the complete and orthogonal basis sets of Hermite- and Laguerre-Gaussian beams. Motivated by the evident inclusion of higher-order modes in free electron laser simulations, a tool is developed for the higher-order (in particular Laguerre-Gaussian) modal analysis of simulated free electron laser beams.

THIS PAGE INTENTIONALLY LEFT BLANK

CONTENTS

I. THE FREE ELECTRON LASER	1
A. SYSTEM	1
B. GENERAL THEORY	3
1. ELECTRON MOTION	3
2. EVOLUTION OF THE OPTICAL MODE	9
3. INTERACTION AND GAIN	12
II. FUNDAMENTAL MODE OPTICS	19
A. PROPAGATION - ANALYTIC DESCRIPTION	19
1. THE PARABOLIC WAVE EQUATION	19
2. SOLVING THE DIMENSIONLESS PARABOLIC WAVE EQUATION	21
B. PROPERTIES OF THE GAUSSIAN BEAM	24
III. MOTIVATION: FREE ELECTRON LASER SIMULATIONS	27
A. MULTIPLE MODES	27
1. MULTI-MODE SIMULATIONS OF A SHORT-RAYLEIGH LENGTH FEL	27
2. RESULTS	28
B. OPTICAL MODE DISTORTION	34
1. OPTICAL MODE DISTORTION IN A SHORT RAYLEIGH LENGTH FEL	34
2. RESULTS	36
C. THE NEED FOR HIGHER-ORDER MODE ANALYSIS	37
IV. HIGHER-ORDER MODES	39
A. HERMITE-GAUSSIAN BEAMS	39
B. LAGUERRE-GAUSSIAN BEAMS	41
C. NUMERICAL PROPAGATION OF HIGHER-ORDER MODES	47
D. POWER ON TARGET	49
E. CONCLUSION	53
APPENDIX: THE PARABOLIC WAVE EQUATION	55
INITIAL DISTRIBUTION LIST	59

THIS PAGE INTENTIONALLY LEFT BLANK

LIST OF FIGURES

1.1	Oscillator FEL	1
1.2	Amplifier FEL	2
1.3	Recirculating free electron laser oscillator.	2
1.4	FEL Gain on Resonance	8
1.5	FEL Gain Off Resonance	8
1.6	FEL Weak Field Gain Curve	16
2.1	Optical Mode Diagram	26
2.2	Propagation of a Gaussian beam.	26
3.1	Output from a 2003 FEL simulation.	29
3.2	Extraction η vs. bunch charge q	30
3.3	Extraction η vs. undulator periods N	31
3.4	Extraction η and optimum initial phase velocity ν_0 vs. normalized electron beam waist radius σ	32
3.5	The interaction region.	32
3.6	Extraction η and mirror intensity vs. normalized Rayleigh length \tilde{z}_0	33
3.7	Output from a 2004 FEL simulation.	35
3.8	Extraction η vs. dimensionless Rayleigh length \tilde{z}_0	36
3.9	Extraction η vs. dimensionless mirror separation τ_{mir}	36
3.10	Optical mode shape suggesting reinforcement by electron beam.	37
4.1	Hermite-Gaussian Modes	41
4.2	Laguerre-Gaussian Modes	43
4.3	Output from bm.c	48
4.4	Output from bm.c	49
4.5	Two functions lead to the same squared function.	49
4.6	Output from bm.c	50
4.7	A combination of LG modes before and after propagation.	50
4.8	Output from bm.c	51
4.9	Output from bm.c	51
4.10	Energy on target for higher-order modes.	51
4.11	Three-dimensional plot of L_1^0	52
4.12	Various beam modes propagating.	52

THIS PAGE INTENTIONALLY LEFT BLANK

LIST OF TABLES

2.1	Symbols Used in the Dimensionless Parabolic Wave Equation	25
3.1	Parameters for a Proposed High-Power FEL	34
4.1	Hermite Polynomials	41
4.2	Laguerre Polynomials	42

THIS PAGE INTENTIONALLY LEFT BLANK

LIST OF SYMBOLS

a	dimensionless optical field strength
\mathbf{A}	vector potential
A_b	electron beam cross sectional area
A_o	optical mode cross sectional area
A^μ	four-vector potential
\mathbf{B}	magnetic field
B_r	optical mode magnetic field magnitude
B_u	undulator magnetic field magnitude
c	speed of light in vacuum
e	electron charge
\mathbf{E}	electric field
E_b	electron beam energy
E_e	electron energy
E_r	optical mode electric field magnitude
F	filling factor
$F^{\alpha\beta}$	field-strength tensor
G	gain
J	current density
j	dimensionless current density
j^μ	four-current density
k	optical wavenumber
k_0	undulator wavenumber
K	undulator parameter
l_b	bunch length
L	undulator length
m	electron mass
N	number of undulator periods
N_e	number of electrons
q	charge
Q	resonator quality factor
r_b	beam radius
t	time
u	electron velocity
U^α	electron four-velocity
V	volume

w	spot size
w_0	spot size at waist
z_0	Rayleigh range
Z_0	dimensionless Rayleigh range
β	dimensionless velocity
γ	Lorentz factor
\hat{e}_k	polarization unit vector
ζ	ponderomotive electron phase
η	extraction
λ	optical wavelength
λ_0	undulator wavelength
ν	dimensionless phase velocity
σ	dimensionless electron beam radius
ρ_e	electron density
τ	dimensionless time
T	proper time
ϕ, ψ	optical phase
ω	optical frequency
ω_0	undulator frequency

CHAPTER I.

THE FREE ELECTRON LASER

In 1971 Stanford University physicist John Madey proposed the development of a coherent light source based on the radiation emitted by relativistic free electrons: a free electron laser.¹ In 1976, his team amplified a CO₂ laser beam using relativistic free electrons from the Stanford Superconducting Linear Accelerator. They later observed coherent infrared radiation at a wavelength of 3 μm in an oscillator configuration. These achievements gave birth to the contemporary free electron laser described below.

A. SYSTEM

The two main components of a free electron laser are an *accelerator* which imparts kinetic energy to a beam of free electrons, and an *undulator* also called a *wiggler* which extracts energy from the beam in the form of coherent radiation. There are a variety of FEL designs; all contain these two essential elements. Varying among individual configurations are the methods by which the electron beam is created, transported, then dumped, and how the radiation is amplified. Some FEL's are amplifiers, some are oscillators. The oscillator

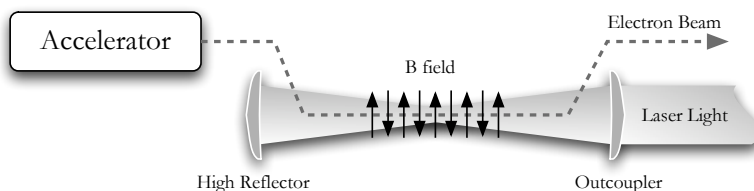


Figure 1.1: Oscillator FEL

configuration is shown in Figure 1.1. Electromagnetic radiation is stored within a resonant cavity, and the increased optical power is outcoupled through a partially-transmitting dielectric. In the amplifier configuration (Figure 1.2), spontaneously emitted light or light from a seed laser is amplified in a single pass through the undulating electron beam.

¹J. M. J. Madey, "Stimulated Emission of Bremsstrahlung in a Periodic Magnetic Field", *Journal of Applied Physics*, Vol. 42, No. 5, pp. 1906-1913, April 1971.

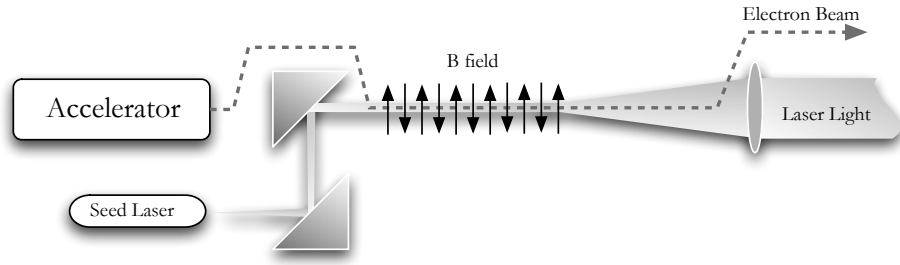


Figure 1.2: Amplifier FEL

The source of free electrons is usually a cathode within an electron gun. Whether configured as an oscillator or amplifier, the electron beam itself may be either recirculated or dumped after exiting the undulator. Recirculation allows the recovery of beam energy back to the accelerator, enhancing overall system efficiency, with the added benefit of dumping less energetic electrons, producing less background radiation. In the RF recovery configuration, electrons return to the accelerator 180° out of phase with respect to those entering from the beam source. Figure 1.3 shows the entire system for a recirculating free electron laser oscillator.

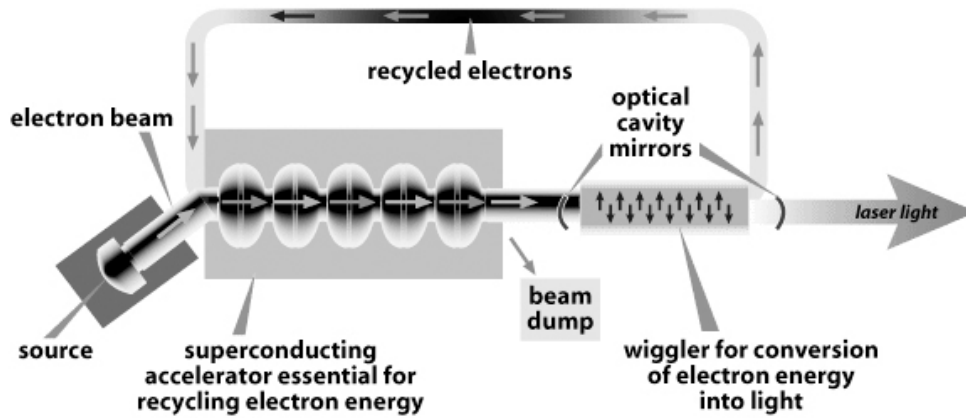


Figure 1.3: Recirculating free electron laser oscillator.

Attributes

The free electron laser's most striking difference from conventional lasers is also its chief advantage. The absence of a vulnerable medium such as a crystal or fluid chemical matrix means that an FEL can achieve extremely high intensity without damaging the laser itself. High wall-plug efficiency ($\sim 10\%$) is predicted for high power FELs with recirculating electron beams. High reliability is also a characteristic: currently operating FELs run continuously and reliably for weeks.

Free electron lasers are continuously tunable. The relativistic Lorentz factor γ of the electron beam, the undulator period λ_0 , and undulator RMS magnetic field strength B_{rms} determine the laser wavelength λ according to the resonance condition²

$$\lambda = \frac{\lambda_0(1 + K^2)}{2\gamma^2}, \quad (1.1)$$

where the undulator parameter K is defined as

$$K = \frac{eB_{\text{rms}}\lambda_0}{2\pi mc^2}. \quad (1.2)$$

Here e is the electron charge, m the mass of the electron, and c the speed of light in vacuum. The relation (1.1) suggests that the undulator wavelength and magnetic field as well as the energy of the electrons³ may be adjusted within an operating laser to yield light over a range of wavelengths. Free electron lasers have been designed to produce radiation from microwaves to X-rays, and they are continuously tunable over a smaller range within these regimes. In addition, the short-pulse nature of the radiation may enhance propagation of optical power through the atmosphere, making the laser particularly suited as a weapon.^{4,5}

B. GENERAL THEORY

Free electron laser theory addresses the motion of the oscillating electrons, the propagation and diffraction of the resulting radiation (the optical mode), and the subsequent interaction of that radiation with the electron beam itself. We forego a discussion of diffraction until the next chapter, and proceed with a description of the electron motion, the optical mode, and gain.

1. ELECTRON MOTION

The trajectory of a relativistic charged particle in external fields is governed by the Lorentz force equation⁶

$$\frac{dU^\alpha}{dT} = \frac{q}{mc} F^{\alpha\beta} U_\beta, \quad (1.3)$$

²At resonance in an FEL, one wavelength of light passes over one electron in one undulator period.

³Tuning via electron beam energy is generally considered more difficult than via undulator geometry. Indeed, significant changes in electron energy require adjustments to guiding and focusing magnets along the entire length of the accelerator.

⁴P. Sprangle, J. R. Peñano and B. Hafizi, “Propagation of Intense Short Laser Pulses in the Atmosphere”, *Phys. Rev. E*, 66, 046418, 2002.

⁵P. Sprangle, J. R. Peñano, A. Ting, B. Hafizi, and D. F. Gordon, “Propagation of Short, High-Intensity Laser Pulses in Air”, *J. Dir. Energy* 1, 73, 2003.

⁶We shall use T for proper time; τ will be used for dimensionless time; cgs units are used throughout this chapter.

where $U^\alpha \equiv (\gamma c, \gamma \mathbf{u})$ is the four-velocity of the particle and

$$F^{\alpha\beta} = \begin{pmatrix} 0 & -E_x & -E_y & -E_z \\ E_x & 0 & -B_z & B_y \\ E_y & B_z & 0 & -B_x \\ E_z & -B_y & B_x & 0 \end{pmatrix} \quad (1.4)$$

is the field-strength tensor, whose components are given by the periodic magnetic field of the undulator and the electric and magnetic components of the radiation field. For the propagation of a plane wave along the z -axis of a helical undulator,⁷ the undulator and radiation fields are taken to be

$$\mathbf{B}_u = B_0(\cos k_0 z, \sin k_0 z, 0), \quad (1.5a)$$

$$\mathbf{E}_r = E(\cos \psi, -\sin \psi, 0), \quad (1.5b)$$

$$\mathbf{B}_r = E(\sin \psi, \cos \psi, 0), \quad (1.5c)$$

where B_0 and $k_0 = 2\pi/\lambda_0$ are the amplitude and wavenumber of the undulator field, $E \equiv E(x, y, z, t)$ is the optical field amplitude, and the phase is $\psi \equiv kz - \omega t + \phi(z, t)$, where $k = \omega/c$ is the optical wavenumber, and $\phi(z, t)$ is the optical phase. The field-strength tensor is then

$$F^{\alpha\beta} = \begin{pmatrix} 0 & -E \cos \psi & E \sin \psi & 0 \\ E \cos \psi & 0 & 0 & B_0 \sin k_0 z + E \cos \psi \\ -E \sin \psi & 0 & 0 & -B_0 \cos k_0 z - E \sin \psi \\ 0 & -B_0 \sin k_0 z - E \cos \psi & B_0 \cos k_0 z + E \sin \psi & 0 \end{pmatrix}. \quad (1.6)$$

Inserting (1.6) into (1.3) gives the four coupled differential equations

$$\frac{dU^0}{dT} = -\frac{e}{mc} (U^1 E \cos \psi - U^2 E \sin \psi), \quad (1.7a)$$

$$\frac{dU^1}{dT} = -\frac{e}{mc} [U^0 E \cos \psi - U^3 (B_0 \sin k_0 z + E \cos \psi)], \quad (1.7b)$$

$$\frac{dU^2}{dT} = -\frac{e}{mc} [-U^0 E \sin \psi - U^3 (-B_0 \cos k_0 z - E \sin \psi)], \quad (1.7c)$$

$$\frac{dU^3}{dT} = -\frac{e}{mc} [-U^1 (-B_0 \sin k_0 z - E \cos \psi) - U^2 (B_0 \cos k_0 z + E \sin \psi)]. \quad (1.7d)$$

Making the substitutions

$$u^i = c\beta^i, \quad (1.8)$$

$$dT = \frac{dt}{\gamma}, \quad (1.9)$$

⁷In a helical undulator, consecutive magnetic fields are rotated 90° from each other causing the electron to follow a corkscrew path. The derivation for electron motion in a linear undulator is more complicated.

where $\gamma = (1 - \boldsymbol{\beta} \cdot \boldsymbol{\beta})^{-1/2}$, we can rewrite (1.7) as

$$\frac{d\gamma}{dt} = -\frac{e}{mc} E (\beta_x \cos \psi - \beta_y \sin \psi), \quad (1.10a)$$

$$\frac{d}{dt}(\gamma\beta_x) = -\frac{e}{mc} [E \cos \psi - \beta_z (B_0 \sin k_0 z + E \cos \psi)], \quad (1.10b)$$

$$\frac{d}{dt}(\gamma\beta_y) = -\frac{e}{mc} [-E \sin \psi - \beta_z (-B_0 \cos k_0 z - E \sin \psi)], \quad (1.10c)$$

$$\frac{d}{dt}(\gamma\beta_z) = -\frac{e}{mc} [E (\beta_x \cos \psi - \beta_y \sin \psi) + B_0 (\beta_x \sin k_0 z - \beta_y \cos k_0 z)]. \quad (1.10d)$$

The magnetic field does no work, and indeed (1.10a) states that the electron's energy is affected only by the coupling of the radiation *electric* field to the electron's transverse motion. It is convenient to rewrite this equation as

$$\dot{\gamma} = -\frac{e}{mc} \boldsymbol{\beta} \cdot \mathbf{E}. \quad (1.11)$$

By defining a transverse velocity $\boldsymbol{\beta}_\perp = \beta_x \hat{\mathbf{x}} + \beta_y \hat{\mathbf{y}} = (\beta_x, \beta_y, 0)$, we may combine (1.10b) and (1.10c) into a single expression

$$\frac{d(\gamma\boldsymbol{\beta}_\perp)}{dt} = -\frac{e}{mc} [E (1 - \beta_z) (\cos \psi, -\sin \psi, 0) + \beta_z B_0 (-\sin k_0 z, \cos k_0 z, 0)] \quad (1.12)$$

which for highly relativistic electrons ($\beta_z \rightarrow 1$) can be approximated by

$$\frac{d(\gamma\boldsymbol{\beta}_\perp)}{dt} \approx -\frac{e}{mc} [\beta_z B_0 (-\sin k_0 z, \cos k_0 z, 0)]. \quad (1.13)$$

Equation (1.13) is readily integrated:

$$\int d(\gamma\boldsymbol{\beta}_\perp) = -\frac{eB_0}{mc} \int \beta_z (-\sin k_0 z, \cos k_0 z, 0) dt, \quad (1.14)$$

$$\gamma\boldsymbol{\beta}_\perp = -\frac{eB_0}{mc^2} \int \frac{dz}{\mathcal{A}} (-\sin k_0 z, \cos k_0 z, 0) \mathcal{A}, \quad (1.15)$$

$$\begin{aligned} \boldsymbol{\beta}_\perp &= -\frac{eB_0}{k_0 \gamma mc^2} (\cos k_0 z, \sin k_0 z, 0) + \mathbf{C} \\ &= -\frac{eB_0 \lambda_0}{2\pi \gamma mc^2} (\cos k_0 z, \sin k_0 z, 0) + \mathbf{C}. \end{aligned} \quad (1.16)$$

We eliminate the constant of integration by assuming perfect injection, so that

$$\boldsymbol{\beta}_\perp(0) = -\frac{eB_0 \lambda_0}{2\pi \gamma mc^2}. \quad (1.17)$$

Using (1.2) and the fact that for a helical undulator $B_{\text{rms}} = B_0$, we can write

$$\boldsymbol{\beta}_\perp = -\frac{K}{\gamma} (\cos k_0 z, \sin k_0 z, 0) \quad (1.18)$$

or

$$\beta_x = -\frac{K}{\gamma} \cos k_0 z, \quad (1.19)$$

$$\beta_y = -\frac{K}{\gamma} \sin k_0 z. \quad (1.20)$$

Substituting (1.18) into (1.11), we have

$$\begin{aligned} \dot{\gamma} &= \frac{eKE}{\gamma mc} (\cos k_0 z, \sin k_0 z, 0) \cdot (\cos \psi, -\sin \psi, 0) \\ &= \frac{eKE}{\gamma mc} (\cos k_0 z \cos \psi - \sin k_0 z \sin \psi) \\ &= \frac{eKE}{\gamma mc} \cos(k_0 z + \psi). \end{aligned} \quad (1.21)$$

Meanwhile, substituting (1.19) and (1.20) into (1.10d) gives us

$$\begin{aligned} \frac{d}{dt}(\gamma\beta_z) &= -\frac{e}{mc} \left[E \left(-\frac{K}{\gamma} \cos k_0 z \cos \psi + \frac{K}{\gamma} \sin k_0 z \sin \psi \right) \right. \\ &\quad \left. + B_0 \left(-\frac{K}{\gamma} \cos k_0 z \sin k_0 z + \frac{K}{\gamma} \sin k_0 z \cos k_0 z \right) \right], \end{aligned} \quad (1.22)$$

$$\begin{aligned} \dot{\gamma}\beta_z + \gamma\dot{\beta}_z &= \frac{eK}{\gamma mc} [E (\cos k_0 z \cos \psi - \sin k_0 z \sin \psi) \\ &\quad - B_0 (\cos k_0 z \sin k_0 z - \sin k_0 z \cos k_0 z)], \end{aligned} \quad (1.23)$$

$$\gamma\dot{\beta}_z = \frac{eKE}{\gamma mc} \cos(k_0 z + \psi) - \dot{\gamma}\beta_z. \quad (1.24)$$

Substituting (1.21) into (1.24), we have

$$\gamma\dot{\beta}_z = \frac{eKE}{\gamma mc} \cos(k_0 z + \psi) - \frac{eKE}{\gamma mc} \cos(k_0 z + \psi)\beta_z, \quad (1.25)$$

$$\gamma\dot{\beta}_z = (1 - \beta_z) \frac{eKE}{\gamma mc} \cos(k_0 z + \psi), \quad (1.26)$$

$$\dot{\beta}_z = (1 - \beta_z) \frac{eKE}{\gamma^2 mc} \cos(k_0 z + \psi). \quad (1.27)$$

It is useful at this point to collect the electron terms in $k_0 z + \psi$ by identifying the electron phase

$$\zeta = (k + k_0)z - \omega t, \quad (1.28)$$

referenced to the combined optical and undulator fields. This leads to

$$k_0 z + \psi = \zeta + \phi. \quad (1.29)$$

and

$$\begin{aligned} \dot{\zeta} &= (k + k_0) \frac{dz}{dt} - \omega \\ &= (k + k_0)\beta_z c - \omega. \end{aligned} \quad (1.30)$$

Solving for β_z gives

$$\beta_z = \frac{\dot{\zeta} + \omega}{(k + k_0)c}, \quad (1.31)$$

$$\dot{\beta}_z = \frac{\ddot{\zeta}}{(k + k_0)c}. \quad (1.32)$$

The expression for β_z may be simplified as follows: for laser light we require

$$\omega = \frac{2\pi c}{\lambda} \sim 10^{15} \text{ s}^{-1}. \quad (1.33)$$

Meanwhile, the change in electron phase over the course of the undulator⁸ is

$$\dot{\zeta} \sim \frac{2\pi c}{\lambda_0} \sim 10^9 \text{ s}^{-1}. \quad (1.34)$$

In other words, since typically $\lambda_0 \gg \lambda$, then $\omega \gg \dot{\zeta}$ and (1.31) becomes

$$\beta_z = \frac{\omega}{(k + k_0)c}. \quad (1.35)$$

Using (1.29), (1.32), and (1.35), we may now rewrite (1.27) as

$$\frac{\ddot{\zeta}}{(k + k_0)c} = \frac{eKE}{\gamma^2 mc} \left[1 - \frac{\omega}{(k + k_0)c} \right] \cos(\zeta + \phi), \quad (1.36)$$

$$\begin{aligned} \ddot{\zeta} &= \frac{eKE}{\gamma^2 mc} [(k + k_0)c - \omega] \cos(\zeta + \phi) \\ &= \frac{eKEk_0}{\gamma^2 m} \cos(\zeta + \phi). \end{aligned} \quad (1.37)$$

We can normalize the evolution of the electron motion to the length of the undulator by defining a dimensionless time $\tau = ct/L$. We adopt the notation $\overset{\circ}{\zeta} \equiv d\zeta/d\tau$ and we write

$$\begin{aligned} \overset{\circ}{\zeta} &= \frac{eKEk_0L^2}{\gamma^2 mc^2} \cos(\zeta + \phi) \\ &= \frac{2\pi eKEL^2}{\gamma^2 mc^2 \lambda_0} \cos(\zeta + \phi) \\ &= \frac{2\pi NeKEL}{\gamma^2 mc^2} \cos(\zeta + \phi), \end{aligned} \quad (1.38)$$

where $N = L/\lambda_0$ is the number of undulator periods. Defining the dimensionless optical field

$$|a| \equiv \frac{2\pi NeKEL}{\gamma^2 mc^2}, \quad (1.39)$$

⁸To achieve gain, the electrons must “bunch” in phase as they traverse the undulator. This is discussed further in the next two sections.

we have the pendulum equation

$$\ddot{\zeta} = |a| \cos(\zeta + \phi). \quad (1.40)$$

Figures 1.4 and 1.5 show the results of a simple simulation of an operating FEL. The electron trajectories in phase space are indeed of a pendular nature: the paths are elliptical (closed paths, as in Figure 1.4 - the pendulum swings back and forth), and there exists a separatrix, a boundary outside of which change in electron phase ζ does not reverse sign (open paths, as in Figure 1.5 - the pendulum goes “over the top”). These figures will be discussed more in the following sections.

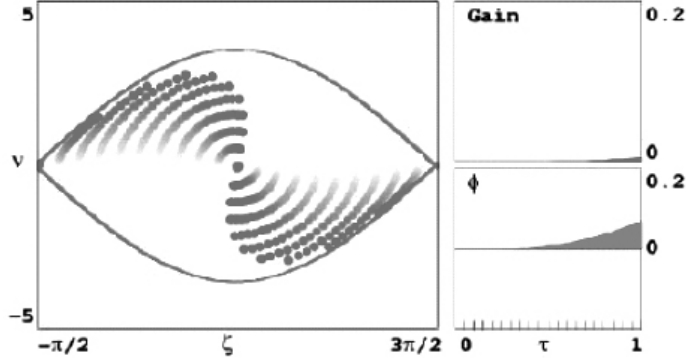


Figure 1.4: Electrons moving in phase space, within the separatrix ($\nu_0 = 0$). Although there is some evolution of the optical phase, there is no significant gain on resonance. (The shading of electrons darkens with increasing τ .)

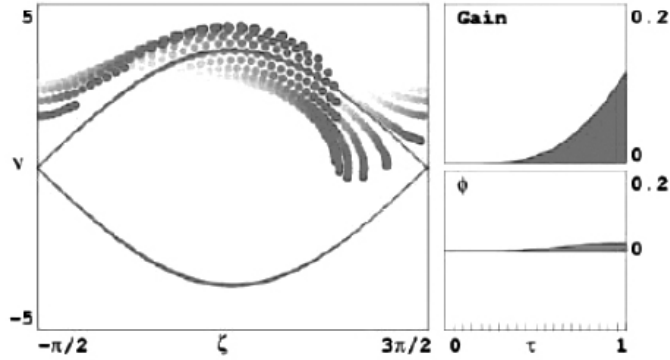


Figure 1.5: Electrons moving outside the separatrix ($\nu_0 = 2.6$). There is gain due to favorable bunching of the electrons in phase space.

2. EVOLUTION OF THE OPTICAL MODE

The fields generated by the oscillating electrons must satisfy the inhomogeneous Maxwell equations

$$\partial_\alpha \mathcal{R}^{\alpha\beta} = \frac{4\pi}{c} J^\beta, \quad (1.41)$$

where

$$\mathcal{R}^{\alpha\beta} = \begin{pmatrix} 0 & -E \cos \psi & E \sin \psi & 0 \\ E \cos \psi & 0 & 0 & E \cos \psi \\ -E \sin \psi & 0 & 0 & -E \sin \psi \\ 0 & -E \cos \psi & E \sin \psi & 0 \end{pmatrix} \quad (1.42)$$

is the radiation part of (1.6), and $J^\alpha \equiv (c\rho, \mathbf{J})$ is the electron beam 4-current. We seek a 4-vector potential $A^\alpha \equiv (\Phi, \mathbf{A})$ satisfying

$$\mathcal{R}^{\alpha\beta} = \partial^\alpha A^\beta - \partial^\beta A^\alpha, \quad (1.43)$$

and the Lorenz condition $\partial_\alpha A^\alpha = 0$, for which (1.41) becomes the wave equation

$$\begin{aligned} \partial_\alpha (\partial^\alpha A^\beta - \partial^\beta A^\alpha) &= \frac{4\pi}{c} J^\beta, \\ \partial_\alpha \partial^\alpha A^\beta - \cancel{\partial^\beta \partial_\alpha A^\alpha} &= \frac{4\pi}{c} J^\beta, \\ \square A^\alpha &= \frac{4\pi}{c} J^\alpha, \end{aligned} \quad (1.44)$$

where $\square \equiv \partial_\alpha \partial^\alpha$ is the d'Alembertian operator. A suitable choice⁹ is

$$A^\alpha = \begin{pmatrix} 0 \\ \frac{E}{k} \sin \psi \\ \frac{E}{k} \cos \psi \\ 0 \end{pmatrix}, \quad (1.45)$$

which gives

$$\partial_\alpha A^\alpha = \frac{\partial}{\partial x} \frac{E}{k} \sin \psi + \frac{\partial}{\partial y} \frac{E}{k} \cos \psi = 0 \quad (1.46)$$

⁹This choice is suitable because it corresponds to a helically polarized wave. A general expression for A^α in terms of the electron 4-velocity is available in the form of the Liénard-Wiechert potentials (see pp. 661-665, J. D. Jackson, *Classical Electrodynamics*, Wiley, New Jersey, 1999). Our choice is made with the benefit of hindsight and is not unique.

and, using $\omega = kc$,

$$\mathcal{R}^{00} = \frac{\partial A^0}{\partial x_0} - \frac{\partial A^0}{\partial x_0} = 0, \quad (1.47a)$$

$$\mathcal{R}^{01} = \frac{\partial A^1}{\partial x_0} - \frac{\partial A^0}{\partial x_1} = \frac{E}{kc} \frac{\partial}{\partial t} \sin \psi = -E \cos \psi, \quad (1.47b)$$

$$\mathcal{R}^{02} = \frac{\partial A^2}{\partial x_0} - \frac{\partial A^0}{\partial x_2} = \frac{E}{kc} \frac{\partial}{\partial t} \cos \psi = E \sin \psi, \quad (1.47c)$$

\vdots

satisfying (1.42). We now write (1.44) as two second-order partial differential equations

$$\frac{1}{c^2} \frac{\partial^2 E}{\partial t^2} \frac{1}{k} \sin \psi - \frac{\partial^2 E}{\partial z^2} \frac{1}{k} \sin \psi = \frac{4\pi}{c} J_x, \quad (1.48a)$$

$$\frac{1}{c^2} \frac{\partial^2 E}{\partial t^2} \frac{1}{k} \cos \psi - \frac{\partial^2 E}{\partial z^2} \frac{1}{k} \cos \psi = \frac{4\pi}{c} J_y. \quad (1.48b)$$

For $E(z, t)$ and $\phi(z, t)$ slowly varying, that is

$$\left| \frac{\partial^2 E}{\partial z^2} \right| \ll \left| k \frac{\partial E}{\partial z} \right|, \quad \left| \frac{\partial^2 E}{\partial t^2} \right| \ll \left| \omega \frac{\partial E}{\partial t} \right|, \quad \left| \frac{\partial^2 \phi}{\partial z^2} \right| \ll \left| k \frac{\partial \phi}{\partial z} \right|, \quad \left| \frac{\partial^2 \phi}{\partial t^2} \right| \ll \left| \omega \frac{\partial \phi}{\partial t} \right|, \quad (1.49)$$

we keep only the boxed terms in

$$\begin{aligned} & \frac{1}{\omega c} \frac{\partial^2 E}{\partial t^2} \sin \psi + \frac{2}{\omega c} \frac{\partial E \partial \phi}{\partial t^2} \cos \psi + \boxed{-\frac{2}{c} \frac{\partial E}{\partial t} \cos \psi} + \frac{E}{\omega c} \frac{\partial^2 \phi}{\partial t^2} \cos \psi - \frac{E}{\omega c} \left(\frac{\partial \phi}{\partial t} \right)^2 \sin \psi \\ & + \boxed{\frac{2E}{c} \frac{\partial \phi}{\partial t} \sin \psi} - \frac{\omega E}{c} \sin \psi - \frac{c}{\omega} \frac{\partial^2 E}{\partial z^2} \sin \psi + \boxed{-2 \frac{\partial E}{\partial z} \cos \psi} - \frac{2c}{\omega} \frac{\partial E \partial \phi}{\partial z^2} \cos \psi \\ & - \frac{cE}{\omega} \frac{\partial^2 E}{\partial z^2} \cos \psi + \frac{\omega E}{c} \sin \psi + \boxed{2E \frac{\partial \phi}{\partial z} \sin \psi} + \frac{\omega E}{c} \left(\frac{\partial \phi}{\partial z} \right)^2 \sin \psi = \boxed{\frac{4\pi}{c} J_x} \end{aligned} \quad (1.50a)$$

and

$$\begin{aligned} & \frac{1}{\omega c} \frac{\partial^2 E}{\partial t^2} \cos \psi - \frac{2}{\omega c} \frac{\partial E \partial \phi}{\partial t^2} \sin \psi + \boxed{\frac{2}{c} \frac{\partial E}{\partial t} \sin \psi} - \frac{E}{\omega c} \frac{\partial^2 \phi}{\partial t^2} \sin \psi - \frac{E}{\omega c} \left(\frac{\partial \phi}{\partial t} \right)^2 \cos \psi \\ & + \boxed{\frac{2E}{c} \frac{\partial \phi}{\partial t} \cos \psi} - \frac{\omega E}{c} \cos \psi - \frac{c}{\omega} \frac{\partial^2 E}{\partial z^2} \cos \psi + \boxed{2 \frac{\partial E}{\partial z} \sin \psi} + \frac{2c}{\omega} \frac{\partial E \partial \phi}{\partial z^2} \sin \psi \\ & + \frac{cE}{\omega} \frac{\partial^2 E}{\partial z^2} \sin \psi + \frac{\omega E}{c} \cos \psi + \boxed{2E \frac{\partial \phi}{\partial z} \cos \psi} + \frac{\omega E}{c} \left(\frac{\partial \phi}{\partial z} \right)^2 \cos \psi = \boxed{\frac{4\pi}{c} J_y}, \end{aligned} \quad (1.50b)$$

leaving

$$2E \left(\frac{1}{c} \frac{\partial \phi}{\partial t} + \frac{\partial \phi}{\partial z} \right) \sin \psi - 2 \left(\frac{1}{c} \frac{\partial E}{\partial t} + \frac{\partial E}{\partial z} \right) \cos \psi = \frac{4\pi}{c} J_x, \quad (1.51a)$$

$$2E \left(\frac{1}{c} \frac{\partial \phi}{\partial t} + \frac{\partial \phi}{\partial z} \right) \cos \psi + 2 \left(\frac{1}{c} \frac{\partial E}{\partial t} + \frac{\partial E}{\partial z} \right) \sin \psi = \frac{4\pi}{c} J_y. \quad (1.51b)$$

Defining $\mathbf{J}_\perp \equiv (J_x, J_y, 0)$, this can be written

$$2 \left(\frac{1}{c} \frac{\partial E}{\partial t} + \frac{\partial E}{\partial z} \right) (-\cos \psi, \sin \psi, 0) + 2E \left(\frac{1}{c} \frac{\partial \phi}{\partial t} + \frac{\partial \phi}{\partial z} \right) (\sin \psi, \cos \psi, 0) = \frac{4\pi}{c} \mathbf{J}_\perp, \quad (1.52)$$

and identifying the orthogonal unit polarization vectors

$$\hat{\mathbf{e}}_1 \equiv (-\cos \psi, \sin \psi, 0) \quad (1.53a)$$

$$\hat{\mathbf{e}}_2 \equiv (\sin \psi, \cos \psi, 0) \quad (1.53b)$$

we can write

$$\left(\frac{\partial E}{\partial t} + c \frac{\partial E}{\partial z} \right) = 2\pi \mathbf{J}_\perp \cdot \hat{\mathbf{e}}_1, \quad (1.54a)$$

$$E \left(\frac{\partial \phi}{\partial t} + c \frac{\partial \phi}{\partial z} \right) = 2\pi \mathbf{J}_\perp \cdot \hat{\mathbf{e}}_2. \quad (1.54b)$$

The operator

$$\begin{aligned} \frac{\partial}{\partial t} + c \frac{\partial}{\partial z} &= \frac{\partial}{\partial t} + \frac{dz}{dt} \frac{\partial}{\partial z} \\ &= \frac{d}{dt} \\ &= \frac{c}{L} \frac{d}{d\tau} \end{aligned} \quad (1.55)$$

is the rate of change in coordinates traveling with the evolving light wave, and we write

$$\frac{dE}{d\tau} = \frac{2\pi L}{c} \mathbf{J}_\perp \cdot \hat{\mathbf{e}}_1, \quad (1.56a)$$

$$E \frac{d\phi}{d\tau} = \frac{2\pi L}{c} \mathbf{J}_\perp \cdot \hat{\mathbf{e}}_2. \quad (1.56b)$$

The transverse current is the sum of individual electron currents, that is

$$\mathbf{J}_\perp = -ec \sum_{i=1}^{N_e} \boldsymbol{\beta}_\perp \delta(\mathbf{x} - \mathbf{r}_i), \quad (1.57)$$

or, using (1.18),

$$\mathbf{J}_\perp = \frac{Kec}{\gamma} \sum_{i=1}^{N_e} \delta(\mathbf{x} - \mathbf{r}_i) (\cos k_0 z, \sin k_0 z, 0). \quad (1.58)$$

Equations (1.56) are then

$$\frac{dE}{d\tau} = \frac{2\pi KeL}{\gamma} \sum_{i=1}^{N_e} \delta(\mathbf{x} - \mathbf{r}_i) (-\cos k_0 z \cos \psi + \sin k_0 z \sin \psi), \quad (1.59a)$$

$$E \frac{d\phi}{d\tau} = \frac{2\pi KeL}{\gamma} \sum_{i=1}^{N_e} \delta(\mathbf{x} - \mathbf{r}_i) (\cos k_0 z \sin \psi + \sin k_0 z \cos \psi), \quad (1.59b)$$

which may be written

$$\frac{dE}{d\tau} = -\frac{2\pi KeLn_e}{\gamma} \int_0^{2\pi} \cos(\zeta + \phi) \frac{d\zeta_0}{2\pi}, \quad (1.60a)$$

$$E \frac{d\phi}{d\tau} = \frac{2\pi KeLn_e}{\gamma} \int_0^{2\pi} \sin(\zeta + \phi) \frac{d\zeta_0}{2\pi}, \quad (1.60b)$$

where n_e is the electron number density, and individual electrons are identified by their initial coordinates in phase space (ζ_0, ν_0) . All electrons are assumed to have the same initial energy ν_0 . These may be combined into

$$\frac{dE}{d\tau} + iE \frac{d\phi}{d\tau} = -\frac{2\pi K e L n_e}{\gamma} \int_0^{2\pi} [\cos(\zeta + \phi) - i \sin(\zeta + \phi)] \frac{d\zeta_0}{2\pi}, \quad (1.61)$$

$$= -\frac{2\pi K e L n_e}{\gamma} \int_0^{2\pi} e^{-i(\zeta + \phi)} \frac{d\zeta_0}{2\pi}. \quad (1.62)$$

Multiplying both sides by $e^{i\phi}$ gives

$$\frac{d}{d\tau} E e^{i\phi} = -\frac{2\pi K e L n_e}{\gamma} \int_0^{2\pi} e^{-i\zeta} \frac{d\zeta_0}{2\pi}. \quad (1.63)$$

A compact form of this expression is found by identifying

$$a \equiv |a| e^{i\phi}, \quad (1.64)$$

$$j \equiv \frac{8\pi^2 K^2 e^2 L^2 N n_e}{\gamma^3 m c^2}, \quad (1.65)$$

where $|a|$ is given by (1.39). Letting an overbar indicate averaging over all initial electron phases, we have

$$\boxed{\bar{a} = -j \overline{e^{-i\zeta}}}. \quad (1.66)$$

It is clear that there is no change in optical field ($da/d\tau = 0$) for $j = 0$. For gain, the integral further requires that the initial phase distribution of electrons average to less than zero. Populations of electrons for which $\overline{e^{-i\zeta}} \neq 0$ are said to be bunched in phase, and the manipulation of electron phase distributions to achieve favorable bunching is a critical concept in FEL design.

3. INTERACTION AND GAIN

We now have expressions for the evolution of the electrons in the undulator (1.40) and the light they create (1.66). To show how this light is amplified, we introduce a solution to (1.40) for weak fields ($|a| \ll \pi$) and low current ($j < \pi$). It is an expansion in a_0 , namely¹⁰

$$\zeta(\tau) = \zeta_0 + \nu_0 \tau - \frac{a_0}{\nu_0^2} [\cos(\zeta_0 + \nu_0 \tau) - \cos(\zeta_0) + \nu_0 \tau \sin(\zeta_0)] + \dots, \quad (1.67)$$

where $\nu \equiv \zeta_0$, a_0 is the initial optical field, and the initial phase is taken to be zero. Thus¹¹

$$\begin{aligned} \nu(\tau) = & \nu_0 + \frac{a_0}{\nu_0} [\sin(\zeta_0 + \nu_0 \tau) - \sin(\zeta_0)] \\ & + \frac{a_0^2}{\nu_0^3} \left\{ -\frac{1}{4} [\cos(2\zeta_0 + 2\nu_0 \tau) - \cos 2\zeta_0] \right. \\ & \left. + \cos \nu_0 \tau - 1 - \nu_0 \tau \sin \zeta_0 \cos(\zeta_0 + \nu_0 \tau) \right\} + \dots \end{aligned} \quad (1.68)$$

¹⁰W. B. Colson, "Free Electron Laser Theory", doctoral dissertation, Stanford University, 1977.

¹¹*Ibid.*

We can use (1.67) and (1.68) to plot the phase space portrait of populations of electrons over their travel time through the undulator, but a more accurate picture is achieved numerically using a computer simulation, such as the one used to generate Figures 1.4 and 1.5.

The amplification of the optical mode is proportional to the energy loss of the electron beam. Leaving (1.68) behind for the moment, we can examine the change in individual electron phase velocity ν by differentiating (1.28):

$$\begin{aligned}\frac{\partial \zeta}{\partial \tau} &= \nu = \frac{\partial}{\partial \tau}[(k + k_0)z - \omega t] \\ &= \frac{L}{c} \left[(k + k_0) \frac{dz}{dt} - \omega \right] \\ &= L[(k + k_0)\beta_z - k],\end{aligned}\tag{1.69}$$

which, assuming $k \gg k_0$, may be approximated

$$\nu = Lk(\beta_z - 1),\tag{1.70}$$

that is

$$\Delta \nu = Lk \Delta \beta_z.\tag{1.71}$$

This is not a surprising expression: change in electron phase velocity is certainly proportional to change in its longitudinal velocity, as the Lorentz force felt by the particle as it passes over each magnet in the undulator depends on this velocity. Moreover, proximity to the resonance condition—most certainly a function of longitudinal electron velocity!—will ultimately determine the gain. Near resonance, we may write (see Equation 1.1):

$$k = \frac{4\pi\gamma^2}{\lambda_0(1 + K^2)},\tag{1.72}$$

thus

$$\begin{aligned}\Delta \nu &= \frac{4\pi L \gamma^2 \Delta \beta_z}{\lambda_0(1 + K^2)} \\ &= \frac{4\pi N \gamma^2 \Delta \beta_z}{1 + K^2}.\end{aligned}\tag{1.73}$$

To put this expression in terms of electron energy, we must re-examine the relationship between β_z and the relativistic γ . In our helical undulator, where (1.18) implies

$$\beta_{\perp}^2 = \frac{K^2}{\gamma^2},\tag{1.74}$$

the definition

$$\gamma = \frac{1}{\sqrt{1 - \boldsymbol{\beta} \cdot \boldsymbol{\beta}}}\tag{1.75}$$

becomes

$$\gamma = \frac{1}{\sqrt{1 - \beta_{\perp}^2 - \beta_z^2}} \quad (1.76)$$

$$= \frac{1}{\sqrt{1 - \frac{K^2}{\gamma^2} - \beta_z^2}}, \quad (1.77)$$

which may be written

$$1 - \beta_z^2 = \frac{1 + K^2}{\gamma^2}, \quad (1.78)$$

and so, taking the differential of each side,

$$\beta_z \Delta \beta_z = \frac{\Delta \gamma (1 + K^2)}{\gamma^3}, \quad (1.79)$$

or

$$\Delta \beta_z = \frac{\Delta \gamma (1 + K^2)}{\beta_z \gamma^3}. \quad (1.80)$$

Plugging this into (1.73) we have

$$\Delta \nu = \frac{4\pi N \Delta \gamma}{\beta_z \gamma}. \quad (1.81)$$

At this point we may return to our approximation $\beta_z \rightarrow 1$ for relativistic electrons, and we write

$$\Delta \nu = 4\pi N \frac{\Delta \gamma}{\gamma}. \quad (1.82)$$

For an electron of energy $E_e = \gamma mc^2$, the energy change as a function of the change in electron phase velocity is then

$$\Delta E_e = \frac{\gamma mc^2}{4\pi N} \Delta \nu. \quad (1.83)$$

Now, the number of electrons in a volume V_b of electron beam is $n_e V_b$. The change in electron beam energy ΔE_b corresponding to V_b is thus

$$\Delta E_b = \frac{n_e \gamma mc^2}{4\pi N} \overline{\Delta \nu} V_b, \quad (1.84)$$

where we have averaged the change in phase velocity for individual electrons. Meanwhile, the optical mode energy E_o in a volume V_o is simply

$$E_o = \frac{E^2}{4\pi} V_o, \quad (1.85)$$

where E is the optical field strength. We now write the optical field gain as

$$G = -\frac{\Delta E_b}{E_o} \quad (1.86)$$

$$\begin{aligned} &= -\frac{n_e \gamma mc^2 V_b \overline{\Delta \nu}}{N E^2 V_o} \\ &= -\frac{n_e \gamma mc^2 F \overline{\Delta \nu}}{N E^2}, \end{aligned} \quad (1.87)$$

where the filling factor F specifies that fraction of the optical mode coincident with the electron beam.¹² Using our definitions for the optical amplitude (1.39) and beam current (1.65), this can be simplified to

$$G = -\frac{2jF}{a_0^2} \overline{\Delta\nu}. \quad (1.88)$$

To find an expression for $\overline{\Delta\nu}$, we return to our weak field expansion of $\nu(\tau)$ (1.68) and integrate over all possible initial electron phases ζ_0 :

$$\begin{aligned} \overline{\Delta\nu} &= \overline{\nu - \nu_0} \\ &= \frac{1}{2\pi} \int_0^{2\pi} (\nu - \nu_0) d\zeta_0 \\ &= \frac{1}{2\pi} \int_0^{2\pi} \left\{ \begin{aligned} &\frac{a_0}{\nu_0} [\sin(\zeta_0 + \nu_0\tau) - \sin(\zeta_0)] \\ &+ \frac{a_0^2}{\nu_0^3} \left\{ -\frac{1}{4} [\cos(2\zeta_0 + 2\nu_0\tau) - \cos 2\zeta_0] \right. \\ &\quad \left. + \cos \nu_0\tau - 1 - \nu_0\tau \sin \zeta_0 \cos(\zeta_0 + \nu_0\tau) \right\} + \dots \end{aligned} \right\} d\zeta_0. \end{aligned} \quad (1.89)$$

Many of the terms average to zero, and so, to second-order in a_0 , we have

$$\overline{\Delta\nu} \approx a_0^2 \left[\frac{2 \cos \nu_0\tau - 2 + \nu_0\tau \sin(\nu_0\tau)}{2\nu_0^3} \right]. \quad (1.90)$$

Plugging this into (1.88) and dividing through by jF , we have

$$\boxed{\frac{G}{jF} = -\frac{2 \cos \nu_0\tau - 2 + \nu_0\tau \sin(\nu_0\tau)}{\nu_0^3}}, \quad (1.91)$$

which describes the FEL gain along the undulator. The final FEL gain at $\tau = 1$ (the end of the undulator) is shown in Figure 1.6. The salient feature of this figure is its antisymmetry, in particular its behavior close to $\nu_0 = 0$,¹³ which indicates that energy may be either transferred from the electron beam to the optical mode ($0 < \nu_0$) or vice-versa ($\nu_0 < 0$). Earlier (see p. 7), we remarked that electrons must bunch in phase space to transfer energy to the optical mode. For a functioning, useful FEL, (1.91) narrows that requirement to a

¹²For electron beam and optical mode volumes both spanning a longitudinal length l , the filling factor is defined as a ratio of cross sectional *areas*:

$$\frac{V_b}{V_o} = \frac{\pi r_b^2 \mathcal{K}}{\pi r_o^2 \mathcal{K}} = \frac{A_b}{A_o}.$$

¹³It is interesting to examine why (1.91) does not blow up at $\nu_0 = 0$. After all, the presence of ν_0^3 in the denominator is certainly suggestive of singular behavior at the origin. The answer is found by expanding

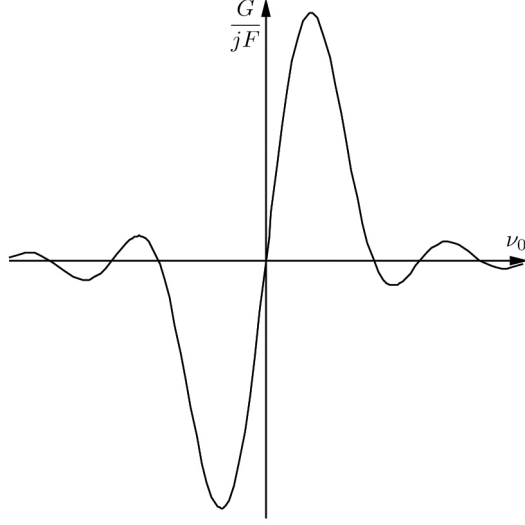


Figure 1.6: The FEL weak field gain curve plotted at the end of the undulator ($\tau = 1$). Energy is either gained by the optical mode or lost, depending on initial phase velocity ν_0 .

population of electrons possessing an average phase velocity just to the positive side of the G/jF axis in Figure 1.6.

To illustrate, we refer once again to Figures 1.4 and 1.5. These show the results of a simple simulation of FEL gain for an electron beam with $\nu_0 = 0$ and $\nu_0 > 0$. In the first case (Figure 1.4), nearly the same amount of energy gained by the optical mode from electrons with decreasing phase velocity is simultaneously lost to electrons whose phase velocity is increasing. In the second case (Figure 1.5), where $\nu_0 > 0$, electrons bunch in the desired region of phase space: they are predominantly losing energy to the optical mode.

the numerator about $\nu_0 = 0$, where

$$\begin{aligned} 2 \cos \nu_0 \tau - 2 + \nu_0 \tau \sin(\nu_0 \tau) &\approx 2 - \nu_0^2 \tau^2 + \frac{\nu_0^4 \tau^4}{12} - 2 + \nu_0 \tau \left(\nu_0 \tau - \frac{\nu_0^3 \tau^3}{6} \right) \\ &= -\frac{\nu_0^4 \tau^4}{12}. \end{aligned}$$

In the vicinity of the origin, then, at $\tau = 0$ (1.91) becomes

$$\frac{G}{jF} = \frac{1}{12} \nu_0,$$

confirmed by the linear nature of the $\nu_0 \approx 0$ region of Figure 1.6.

The introduction of the gain equation completes our preliminary discussion of free electron lasers. For convenience, we review the important conclusions of this chapter: the two principle equations of basic FEL theory, and an expression (derivable from the first) for gain in weak fields.

PENDULUM EQUATION

$$\zeta^{\circ\circ} = |a| \cos(\zeta + \phi) \quad (1.40)$$

WAVE EQUATION

$$\dot{a} = -j \overline{e^{-i\zeta}} \quad (1.66)$$

GAIN EQUATION

(weak fields)

$$\frac{G}{jF} = -\frac{2 \cos \nu_0 \tau - 2 + \nu_0 \tau \sin(\nu_0 \tau)}{\nu_0^3} \quad (1.91)$$

THIS PAGE INTENTIONALLY LEFT BLANK

CHAPTER II.

FUNDAMENTAL MODE OPTICS

The free electron laser is unique among high power lasers in that it operates primarily in the fundamental mode. In contrast, high-power solid state and chemical lasers deliver a beam comprised of many higher-order mode (HOM) components. Over a given propagation range, these HOMs lead to more diffraction loss than, for example, a purely Gaussian beam. While such a beam characterizes the ideal laser, we will show in the next chapter that beams obtained from simulations of FELs appear to contain a few HOMs, and it is our goal to construct a diagnostic tool to evaluate the mode content of a given laser beam whose amplitude and phase are known at every point.

Such comprehensive knowledge of beam makeup is possible in the laboratory with much effort, but a simulation provides all such information *a priori* and allows a comprehensive understanding of the system, and the ability to alter that system, without the high cost of a laboratory experiment. These types of simulations have been benchmarked against actual experiment and have accurately predicted experimental results. Modal analysis, on the other hand, has not been benchmarked, and this analysis provides a starting point for such a comparison.

A. PROPAGATION - ANALYTIC DESCRIPTION

Although we intend to approach the FEL numerically, we are interested in an analytic solution to the wave equation in order to understand the nature of an evolving wavefront inside a laser cavity. For the moment, we consider the optical mode independently of its interaction with the electron beam.

1. THE PARABOLIC WAVE EQUATION

The homogeneous part of (1.44) can be written

$$\left(\nabla^2 - \frac{1}{c^2} \frac{\partial^2}{\partial t^2} \right) \mathbf{A}(\mathbf{x}, t) = 0. \quad (2.1)$$

Expressions solving this equation describe waves propagating in free space (or other homogeneous, sourceless media). Using the same vector potential as in the previous chapter, we

have

$$\mathbf{A}(\mathbf{x}, t) = \Re \left\{ \frac{\mathcal{E}(\mathbf{x}, t)}{k} e^{i\alpha} \hat{\mathbf{e}} \right\} \equiv \frac{E(\mathbf{x}, t)}{k} (\sin \psi, \cos \psi, 0), \quad (2.2)$$

where $\hat{\mathbf{e}} = (-i, 1, 0)$ is the polarization vector, $\alpha = kz - \omega t$ is the carrier wave phase, and $\mathcal{E}(\mathbf{x}, t) = E(\mathbf{x}, t) e^{i\phi(\mathbf{x}, t)}$ is comprised of an amplitude E and phase ϕ now with an explicit transverse dependence (remember that before we used $E \equiv E(z, t)$ and $\phi \equiv \phi(z, t)$; see page 10). To begin substituting this into the wave equation (2.1), we take two derivatives in z and t :

$$\frac{\partial \mathbf{A}}{\partial z} = \Re \left\{ \frac{1}{k} \left(\frac{\partial \mathcal{E}}{\partial z} + ik\mathcal{E} \right) e^{i\alpha} \hat{\mathbf{e}} \right\}, \quad (2.3)$$

$$\frac{\partial^2 \mathbf{A}}{\partial z^2} = \Re \left\{ \frac{1}{k} \left(\frac{\partial^2 \mathcal{E}}{\partial z^2} + 2ik \frac{\partial \mathcal{E}}{\partial z} - k^2 \mathcal{E} \right) e^{i\alpha} \hat{\mathbf{e}} \right\}, \quad (2.4)$$

$$\frac{\partial \mathbf{A}}{\partial t} = \Re \left\{ \frac{1}{k} \left(\frac{\partial \mathcal{E}}{\partial t} - i\omega \mathcal{E} \right) e^{i\alpha} \hat{\mathbf{e}} \right\}, \quad (2.5)$$

$$\frac{\partial^2 \mathbf{A}}{\partial t^2} = \Re \left\{ \frac{1}{k} \left(\frac{\partial^2 \mathcal{E}}{\partial t^2} - 2i\omega \frac{\partial \mathcal{E}}{\partial t} - \omega^2 \mathcal{E} \right) e^{i\alpha} \hat{\mathbf{e}} \right\}. \quad (2.6)$$

As before, for slowly-varying $E(\mathbf{x}, t)$ and $\phi(\mathbf{x}, t)$, variations in amplitude and phase arising from diffraction *in the direction of propagation* are small compared to those of the wave itself, that is

$$\left| \frac{\partial^2 E}{\partial z^2} \right| \ll \left| k \frac{\partial E}{\partial z} \right|, \quad \left| \frac{\partial^2 E}{\partial t^2} \right| \ll \left| \omega \frac{\partial E}{\partial t} \right|, \quad \left| \frac{\partial^2 \phi}{\partial z^2} \right| \ll \left| k \frac{\partial \phi}{\partial z} \right|, \quad \left| \frac{\partial^2 \phi}{\partial t^2} \right| \ll \left| \omega \frac{\partial \phi}{\partial t} \right|. \quad (2.7)$$

These negligible terms comprise the second longitudinal space and time derivatives of \mathcal{E} , which we eliminate to obtain

$$\frac{1}{k} \left[\frac{\partial^2 \mathcal{E}}{\partial x^2} + \frac{\partial^2 \mathcal{E}}{\partial y^2} + \left(2ik \frac{\partial \mathcal{E}}{\partial z} - k^2 \mathcal{E} \right) - \frac{1}{c^2} \left(-2i\omega \frac{\partial \mathcal{E}}{\partial t} - \omega^2 \mathcal{E} \right) \right] e^{i\alpha} \hat{\mathbf{e}} = 0. \quad (2.8)$$

This simplifies to

$$\frac{1}{k} \left[\nabla_{\perp}^2 \mathcal{E} + 2ik \left(\frac{\partial \mathcal{E}}{\partial z} + \frac{1}{c} \frac{\partial \mathcal{E}}{\partial t} \right) \right] e^{i\alpha} \hat{\mathbf{e}} = 0, \quad (2.9)$$

where we have used $\omega = kc$ and introduced the transverse Laplacian

$$\nabla_{\perp}^2 \equiv \frac{\partial^2}{\partial x^2} + \frac{\partial^2}{\partial y^2}. \quad (2.10)$$

Multiplying by $\omega e^{-i\alpha}$, the scalar equation is

$$c \nabla_{\perp}^2 \mathcal{E} + 2ik \left(\frac{\partial \mathcal{E}}{\partial t} + c \frac{\partial \mathcal{E}}{\partial z} \right) = 0, \quad (2.11)$$

and we may once again use (1.55) to write this as

$$\left(\frac{1}{2} \nabla_{\perp}^2 + \frac{ik}{L} \frac{\partial}{\partial \tau} \right) \mathcal{E} = 0. \quad (2.12)$$

With propagation now expressed in terms of τ , we would like to make the diffraction term dimensionless also. The $1/e$ radius w_0 of the initial, fundamental mode of the laser is given by

$$w_0^2 = \frac{z_0 \lambda}{\pi}, \quad (2.13)$$

where z_0 is the Rayleigh length, or the characteristic distance over which the beam cross section increases. Defining the dimensionless transverse coordinates as

$$\tilde{x} = x \sqrt{\frac{\pi}{\lambda L}}, \quad \tilde{y} = y \sqrt{\frac{\pi}{\lambda L}}, \quad (2.14)$$

so that

$$\frac{\partial^2}{\partial x^2} = \frac{k}{2L} \frac{\partial^2}{\partial \tilde{x}^2}, \quad \frac{\partial^2}{\partial y^2} = \frac{k}{2L} \frac{\partial^2}{\partial \tilde{y}^2}, \quad (2.15)$$

and adopting the *dimensionless* transverse Laplacian

$$\tilde{\nabla}_{\perp}^2 = \frac{\partial^2}{\partial \tilde{x}^2} + \frac{\partial^2}{\partial \tilde{y}^2}, \quad (2.16)$$

we now write the dimensionless parabolic¹ wave equation

$$\boxed{\left(-\frac{i}{4} \tilde{\nabla}_{\perp}^2 + \frac{\partial}{\partial \tau}\right) \mathcal{E} = 0}. \quad (2.17)$$

2. SOLVING THE DIMENSIONLESS PARABOLIC WAVE EQUATION

To solve (2.17), we attempt a trial solution of the Gaussian form²

$$\mathcal{E}(\tilde{x}, \tilde{y}, \tau) = \mathcal{E}_0 p(\tau) \exp\left(-\frac{\tilde{x}^2 + \tilde{y}^2}{q(\tau)}\right), \quad (2.18)$$

where $p(\tau)$ and $q(\tau)$ are as yet undetermined complex functions describing the evolution of amplitude and width over dimensionless time. We further impose the initial condition

$$\mathcal{E}(\tilde{x}, \tilde{y}, 0) = \mathcal{E}_0 \exp\left(-\frac{\tilde{x}^2 + \tilde{y}^2}{\tilde{z}_0}\right), \quad (2.19)$$

¹The terms *paraxial* and *parabolic* may both be used to describe (2.17). It is paraxial in that it accurately describes wave behavior close to the axis of propagation. It is parabolic in that it fits into a class of partial differential equations of the general form

$$A \frac{\partial^2 u}{\partial x^2} + 2B \frac{\partial^2 u}{\partial x \partial y} + C \frac{\partial^2 u}{\partial y^2} + D \frac{\partial u}{\partial x} + E \frac{\partial u}{\partial y} + Fu = R(x, y),$$

where

$$\begin{vmatrix} A & B \\ B & C \end{vmatrix} \equiv AC - B^2 = 0.$$

This class of equations includes the Schrödinger equation, with which the parabolic wave equation shares many properties. In contrast, the original wave equation is hyperbolic, that is $AC - B^2 < 0$.

²A spherical wave is a known solution to the wave equation. A Gaussian wavefront may be described as a *paraxial* spherical wave, an approximate solution to the wave equation. It is also, in fact, an *exact* solution to the *paraxial* wave equation.

where $\tilde{z}_0 \equiv \tilde{w}_0^2$ is the *dimensionless* Rayleigh length and the central field amplitude is $\mathcal{E}_0 \equiv \mathcal{E}(0, 0, 0)$. Substituting (2.18) into (2.17), we take the appropriate derivatives in \tilde{x} , \tilde{y} , and τ (letting $\tilde{r}^2 = \tilde{x}^2 + \tilde{y}^2$ and suppressing the argument τ):

$$\frac{\partial^2 \mathcal{E}}{\partial \tilde{x}^2} = \left(\frac{4\tilde{x}^2}{q^2} - \frac{2}{q} \right) \mathcal{E}_0 p e^{-\tilde{r}^2/q}, \quad (2.20)$$

$$\frac{\partial^2 \mathcal{E}}{\partial \tilde{y}^2} = \left(\frac{4\tilde{y}^2}{q^2} - \frac{2}{q} \right) \mathcal{E}_0 p e^{-\tilde{r}^2/q}, \quad (2.21)$$

$$\frac{\partial \mathcal{E}}{\partial \tau} = \left(\frac{1}{p} \frac{dp}{d\tau} + \frac{\tilde{r}^2}{q^2} \frac{dq}{d\tau} \right) \mathcal{E}_0 p e^{-\tilde{r}^2/q}, \quad (2.22)$$

and write

$$\left(\frac{4\tilde{x}^2}{q^2} - \frac{2}{q} \right) \mathcal{E}_0 p e^{-\tilde{r}^2/q} + \left(\frac{4\tilde{y}^2}{q^2} - \frac{2}{q} \right) \mathcal{E}_0 p e^{-\tilde{r}^2/q} + 4i \left(\frac{1}{p} \frac{dp}{d\tau} + \frac{\tilde{r}^2}{q^2} \frac{dq}{d\tau} \right) \mathcal{E}_0 p e^{-\tilde{r}^2/q} = 0. \quad (2.23)$$

Dividing through by $4\mathcal{E}_0 p e^{-\tilde{r}^2/q}$ and collecting terms, we have

$$\frac{\tilde{r}^2}{q^2} - \frac{1}{q} + i \left(\frac{1}{p} \frac{dp}{d\tau} + \frac{\tilde{r}^2}{q^2} \frac{dq}{d\tau} \right) = 0, \quad (2.24)$$

which may be written³

$$\left(\frac{dq}{d\tau} - i \right) \tilde{r}^2 + \left(\frac{1}{p} \frac{dp}{d\tau} + \frac{i}{q} \right) q^2 = 0. \quad (2.25)$$

For this equation to hold for all \tilde{r} (that is, for all \tilde{x} and \tilde{y}), the expressions in parentheses must be identically zero, thus

$$\frac{dq}{d\tau} = i, \quad (2.26)$$

$$\frac{dp}{d\tau} = -i \frac{p}{q}. \quad (2.27)$$

It is easy enough to solve (2.26) for $q(\tau)$:

$$q(\tau) = q_0 + i\tau. \quad (2.28)$$

We are not surprised to find that it is complex, as it must describe not only the evolution of the transverse extent of the wave, but also the evolution of the phase, which must oscillate. From our initial conditions, we find

$$q_0 = \tilde{z}_0, \quad (2.29)$$

also anticipated. Using this result and substituting (2.28) into (2.27), we have,

$$\begin{aligned} \frac{dp}{d\tau} &= -\frac{ip}{\tilde{z}_0 + i\tau} \\ &= \frac{p}{i\tilde{z}_0 - \tau}, \end{aligned} \quad (2.30)$$

³To get from (2.24) to (2.25), multiply through by $-iq^2$, then collect terms in \tilde{r}^2 and q^2 .

which we solve for $p(\tau)$:

$$\begin{aligned}
\ln p &= \int_0^\tau \frac{d\tau'}{i\tilde{z}_0 - \tau'} \\
&= \ln(i\tilde{z}_0 - \tau') \Big|_\tau^0 \\
&= \ln(i\tilde{z}_0) - \ln(i\tilde{z}_0 - \tau) \\
&= \ln \left(\frac{1}{1 + i\frac{\tau}{\tilde{z}_0}} \right), \tag{2.31}
\end{aligned}$$

thus

$$p(\tau) = \frac{1}{1 + i\frac{\tau}{\tilde{z}_0}}. \tag{2.32}$$

What does it mean for $p(\tau)$ to be complex? Our solution to the parabolic wave equation is now

$$\mathcal{E}(\tilde{x}, \tilde{y}, \tau) = \frac{\mathcal{E}_0}{1 + i\frac{\tau}{\tilde{z}_0}} \exp \left(-\frac{\tilde{x}^2 + \tilde{y}^2}{\tilde{z}_0 + i\tau} \right). \tag{2.33}$$

Once again letting $\tilde{r}^2 = \tilde{x}^2 + \tilde{y}^2$, we elucidate this expression by making the following definition:

$$\mathfrak{z} \equiv 1 + i\mu, \tag{2.34}$$

where

$$\mu \equiv \frac{\tau}{\tilde{z}_0}, \tag{2.35}$$

and we write

$$\begin{aligned}
\mathcal{E}(\tilde{x}, \tilde{y}, \tau) &= \frac{\mathcal{E}_0}{\mathfrak{z}} \exp \left(-\frac{\tilde{r}^2}{\tilde{z}_0 \mathfrak{z}} \right) \\
&= \frac{\mathcal{E}_0}{\mathfrak{z}} \exp \left(-\frac{\tilde{r}^2}{\tilde{z}_0} \frac{\mathfrak{z}^*}{\mathfrak{z} \mathfrak{z}^*} \right) \\
&= \frac{\mathcal{E}_0}{\mathfrak{z}} \exp \left[-(1 - i\mu) \frac{\tilde{r}^2}{\tilde{z}_0 \mathfrak{z} \mathfrak{z}^*} \right] \\
&= \frac{\mathcal{E}_0}{\mathfrak{z}} \exp \left(-\frac{\tilde{r}^2}{\tilde{z}_0 \mathfrak{z} \mathfrak{z}^*} + i\mu \frac{\tilde{r}^2}{\tilde{z}_0 \mathfrak{z} \mathfrak{z}^*} \right) \\
&= \frac{\mathcal{E}_0}{\mathfrak{z}} \exp \left(-\frac{\tilde{r}^2}{\tilde{z}_0 \mathfrak{z} \mathfrak{z}^*} \right) \exp \left(i\mu \frac{\tilde{r}^2}{\tilde{z}_0 \mathfrak{z} \mathfrak{z}^*} \right). \tag{2.36}
\end{aligned}$$

Now, the complex number \mathfrak{z} has modulus

$$|\mathfrak{z}| = \sqrt{1 + \mu^2}, \tag{2.37}$$

and argument

$$\arg \mathfrak{z} = \arctan \mu, \quad (2.38)$$

so we may write

$$\frac{1}{\mathfrak{z}} = \frac{e^{-i \arctan \mu}}{\sqrt{1 + \mu^2}}, \quad (2.39)$$

and (2.36) becomes

$$\mathcal{E}(\tilde{x}, \tilde{y}, \tau) = \frac{\mathcal{E}_0}{\sqrt{1 + \mu^2}} \exp\left(-\frac{\tilde{r}^2}{\tilde{z}_0(1 + \mu^2)}\right) \exp\left(i\mu \frac{\tilde{r}^2}{\tilde{z}_0(1 + \mu^2)}\right) e^{-i \arctan \mu}. \quad (2.40)$$

Defining the *dimensionless* beam width

$$\tilde{w} = \sqrt{\tilde{z}_0 \mathfrak{z} \mathfrak{z}^*} = \sqrt{\tilde{z}_0 (1 + \mu^2)} = \sqrt{\tilde{z}_0 \left(1 + \frac{\tau^2}{\tilde{z}_0^2}\right)}, \quad (2.41)$$

we arrive at

$$\mathcal{E}(\tilde{x}, \tilde{y}, \tau) = \mathcal{E}_0 \frac{\tilde{w}_0}{\tilde{w}(\tau)} \exp\left(-\frac{\tilde{r}^2}{\tilde{w}^2(\tau)}\right) \exp\left(i \frac{\tilde{r}^2 \tau}{\tilde{z}_0^2 + \tau^2}\right) \exp\left(-i \arctan \frac{\tau}{\tilde{z}_0}\right), \quad (2.42)$$

where

$$\tilde{w}_0 \equiv \tilde{w}(0) = \sqrt{\tilde{z}_0}. \quad (2.43)$$

This is the solution for the dimensionless parabolic wave equation. Using

$$\phi(\tilde{r}, \tau) \equiv \frac{\tilde{r}^2 \tau}{\tilde{z}_0^2 + \tau^2} - \arctan \frac{\tau}{\tilde{z}_0}, \quad (2.44)$$

we write finally

$$\boxed{\mathcal{E}(\tilde{x}, \tilde{y}, \tau) = \mathcal{E}_0 \frac{\tilde{w}_0}{\tilde{w}(\tau)} e^{-\tilde{r}^2/\tilde{w}^2(\tau)} e^{i\phi(\tilde{r}, \tau)}}. \quad (2.45)$$

B. PROPERTIES OF THE GAUSSIAN BEAM

We have identified a physical basis for each of the factors in (2.45); these are reviewed in Table 2.1. Figure 2.1 illustrates a beam diffracting from a waist at $\tau = 0$ in the $\pm\tau$ directions, identifying the important parameters used in the Gaussian beam expression. We can study the behavior of the beam described by this expression by looking at its variables in their limits. As we have required, at $\tau = 0$,

$$\mathcal{E}(\tilde{x}, \tilde{y}, 0) = \mathcal{E}_0 e^{-\tilde{r}^2/\tilde{z}_0}. \quad (2.46)$$

As τ increases, so does \tilde{w} : the beam expands. For a given \tilde{r} , the overall value on the right hand side of (2.45) decreases with increasing τ : the field strength attenuates.

Figure 2.2 shows a Gaussian beam propagating through free space. The expansion and attenuation of the beam are evident. Also evident is that the Gaussian beam retains its functional form: there is a scaling of the overall structure, but the wavefront remains Gaussian

Table 2.1: Symbols Used in the Dimensionless Parabolic Wave Equation

SYMBOL	DEFINITION	DESCRIPTION (DIMENSIONLESS)
\tilde{x}	$x\sqrt{\frac{\pi}{\lambda L}}$	orthogonal transverse coordinate
\tilde{y}	$y\sqrt{\frac{\pi}{\lambda L}}$	orthogonal transverse coordinate
\tilde{r}	$r\sqrt{\frac{\pi}{\lambda L}} = \frac{r}{\tilde{w}_L}$	transverse coordinate
τ	$\frac{ct}{L}$	time
\tilde{w}	$\sqrt{\tilde{z}_0 \left(1 + \frac{\tau^2}{\tilde{z}_0^2}\right)}$	beam width
\tilde{w}_0	$\tilde{w}(0) = \sqrt{\tilde{z}_0}$	beam width at beam waist
\tilde{z}_0	$\frac{z_0}{L}$	Rayleigh length

after propagation. This behavior is unique to unmixed, individual component solutions of the paraxial wave equation, but as we will show in Chapter IV., the equation allows solutions beyond just the fundamental Gaussian. Moreover, we will show that an arbitrary laser (for example, a laser with a top-hat or annular or just very “messy” cross-sectional wavefront structure) experiences the inclusion of higher-order modes—that is, higher-order solutions to the wave equation—as a loss mechanism⁴ during propagation.

The above claim demands to be addressed, but to further motivate our discussion of higher-order modes, we first present the results of past research in the field of high-power free electron lasers.

⁴This is not loss in the sense of absorption or scattering, but rather with respect to the amount of energy intended to reach a target area.

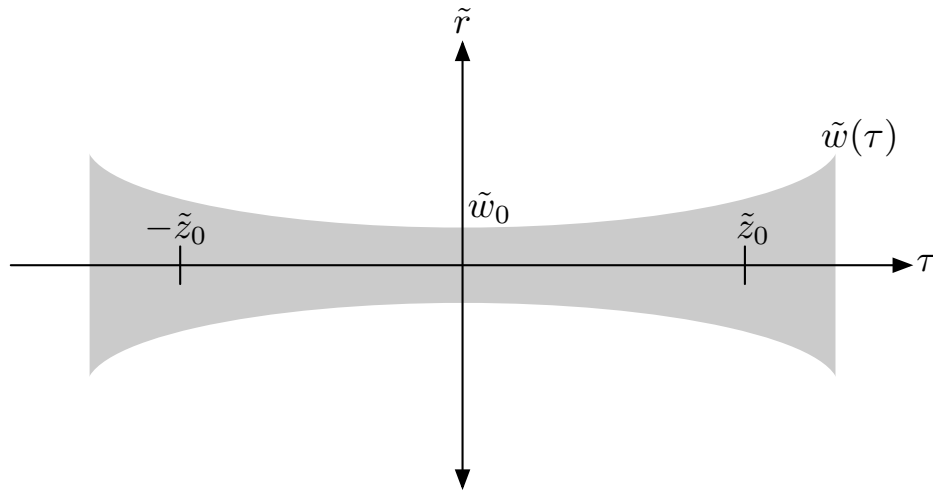


Figure 2.1: A diagram of the optical mode showing the relevant (dimensionless) physical meanings of the symbols in Table 2.1.

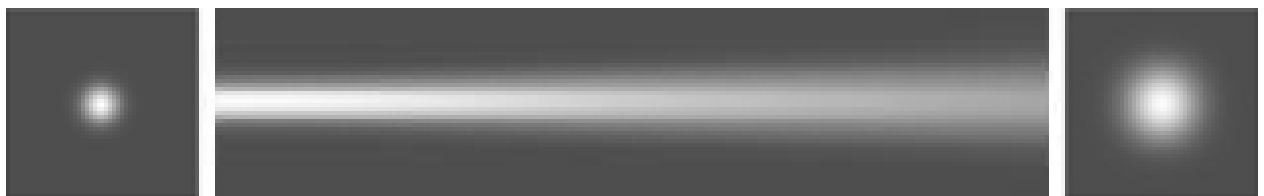


Figure 2.2: The beam described in Figure 2.1 on the interval $0 \leq \tau \leq 1$. The initial Gaussian wavefront (left) propagates through a uniform sourceless medium (center), diffracting into a wider Gaussian of lower peak amplitude (right).

CHAPTER III.

MOTIVATION: FREE ELECTRON LASER SIMULATIONS

A computer simulation of laser beam propagation through a sourceless medium was used to generate Figure 2.2. Such a simulation implements a relatively simple numerical method for solving the parabolic wave equation. More relevant simulations (to wit: the inclusion of the radiation source—the electron beam!) are the work of the Free Electron Laser Research Group. Naval Postgraduate School FEL simulations have been in use for fifteen years and have been useful tools in the construction of new, more powerful FELs. Recently, ever increasing computing speed and power and advances in simulation technology (better codes) have resulted in greater fidelity, and more robust analysis of the evolving FEL system. The inclusion of expanding coordinates and methods of characterizing optical beam quality are among the improvements found in the following work, completed over the last two years.

A. MULTIPLE MODES

Under optimum conditions, the free electron laser operates in the fundamental mode. In order to create the laser beam, the gain medium—a beam of free electrons—passes through the undulator, and thus some portion of the optical cavity. The complicated boundary conditions introduced by the presence of a region of swiftly moving charges within the region of propagation argue strongly for the use of numerical methods. But one might guess that the simple evolution of an initially Gaussian wavefront like that in Figure 2.2 is made more complicated by the presence of the electrons, and in fact simulations that include the electron beam show that *an initially Gaussian FEL beam wavefront can assume an other-than-Gaussian transverse structure.*

1. MULTI-MODE SIMULATIONS OF A SHORT-RAYLEIGH LENGTH FEL

Simulations offer the ability to test variations in free electron laser design parameters such as undulator length, electron bunch charge, and Rayleigh length, before such designs are realized. For a weapon-class FEL, two main objectives are maximizing output power and minimizing the possibility of damage to resonator optics. In 2003, the FEL Group simulated

the performance of a proposed 1 μm high-power FEL with a Rayleigh length an order of magnitude shorter than typical extant operating FELs.¹ The three-dimensional simulation (in \tilde{x} , \tilde{y} , and τ) used self-consistent FEL pendulum (1.40) and wave (1.66) equations to follow the evolution of weak optical fields to steady state, allowing for the development of transverse structure in the wavefront. For simulations of this type, the value of interest is the extraction η , defined as

$$\eta = \frac{\text{extracted optical power}}{\text{initial electron beam power}}. \quad (3.1)$$

More specifically, there are two expressions for η in basic FEL theory:² one for the low gain regime ($j \lesssim 1$),

$$\eta \approx \frac{1}{2N}, \quad (3.2)$$

and one for high gain ($j \gg 1$),

$$\eta \approx \frac{\sqrt[3]{j/2}}{8N}. \quad (3.3)$$

Both are approximate, as is the definition of the cut-off between high and low gain.

In the simulations, design parameters are independently varied to determine their optimum values with η as a gauge. The simulations must determine the optimum resonance parameter

$$\nu_0 = L[(k + k_0)\beta_{z0} - k], \quad (3.4)$$

where L is the undulator length, k is the optical wavenumber, k_0 is the undulator wavenumber, and β_{z0} is the initial electron velocity (see Chapter 1 for details of these parameters). An actual FEL operates at the optimum ν_0 , finding it by automatically varying $\lambda = 2\pi/k$ until a fixed value of ν_0 dominates by mode competition.

2. RESULTS

Each individual simulation run results in output like that shown in Figure 3.1. A series of runs are inspected to determine the optimum ν_0 for a given parameter, say charge q per electron bunch. The plot of extraction η versus q at each optimum ν_0 shown in Figure 3.2 is thus the result of more than one hundred simulation runs. Figure 3.2 demonstrates the steady increase in extraction with increasing bunch charge. The simulation assumes a constant longitudinal emittance

$$\varepsilon_l = \Delta\gamma l_b, \quad (3.5)$$

where $\Delta\gamma$ is the rms spread in the electron energies and l_b is the rms electron bunch length. In a real FEL (and in later simulations), emittance increases with bunch charge, reducing extraction as the beam quality degrades. But the effect is estimated as small here.³

¹W. B. Colson, et al, "Multi-mode Simulations of a Short-Rayleigh Length FEL", *Proceedings, 25th International FEL Conference*, Tsukuba, Japan, September 2003.

²W. B. Colson in W. B. Colson, C. Pellegrini, A. Renieri (Eds.), *Laser Handbook, Vol. 6*, North Holland, Amsterdam, 1990.

³For a concise description of experimental FEL performance as it relates to particular phenomena, such as electron beam emittance, see Chapter 3 of B. W. Williams, *Jefferson Lab Free Electron Laser 10 kW*

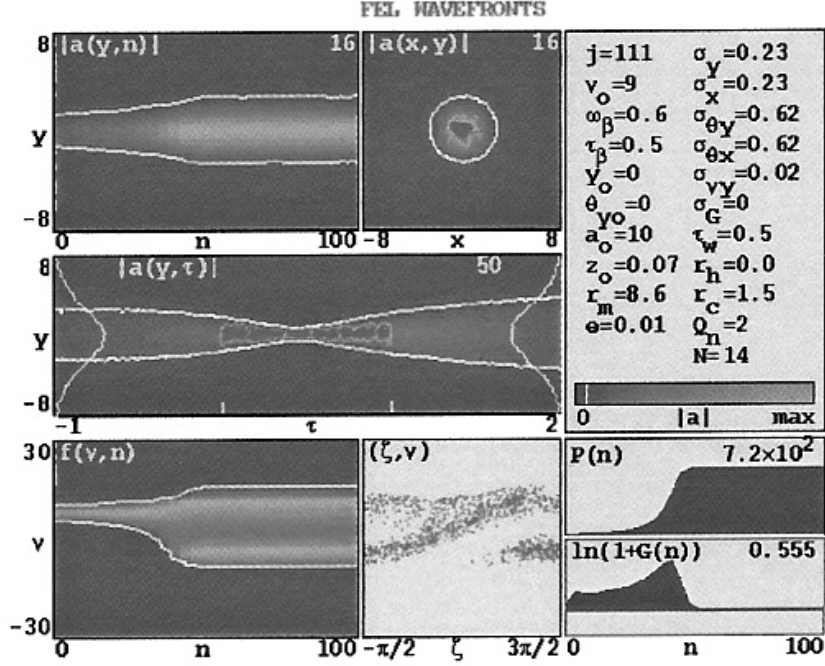


Figure 3.1: Output from a 2003 simulation. Each output figure displays 8 panels showing, clockwise from top left: (1) a plot of the mode evolution over many passes through the undulator, (2) a cross section of the laser beam, (3) a list of input and calculated parameters, (4) a plot of output beam power evolution, (5) a plot of gain evolution, (6) the final phase space portrait of the electrons, (7) an historical plot of electron phase space evolution, and (8) a plot of the mode evolution over the final pass through the undulator.

The results of the 2003 runs, which were presented at the International Free Electron Laser Conference in Tsukuba, Japan, included determinations of optimum number of undulator periods ($N = 14$, see Figure 3.3), optimum normalized beam waist radius ($\sigma = 0.12$, see Figure 3.4), and constraints on normalized Rayleigh length ($\tilde{z}_0 < 0.06$, versus the typical 0.5 in use at the time, see Figure 3.6) and mirror transmission losses ($>50\%$) for the proposed laser.

Figure 3.3 reflects two important FEL design concepts. The first is that too few undulator periods result in a non-functioning FEL, indicated by the rapid drop off in extraction for $N < 10$. This is evident from our definition of the dimensionless current density

$$\begin{aligned}
 j &= \frac{8\pi^2 K^2 e^2 L^2 N n_e}{\gamma^3 m c^2} \\
 &= \frac{8\pi^2 K^2 e^2 \lambda_0^2 N^3 n_e}{\gamma^3 m c^2}.
 \end{aligned} \tag{3.6}$$

Since gain G is proportional to current j , we ultimately have

$$G \propto j \propto N^3. \tag{3.7}$$

Upgrade - Lessons Learned, Technical Report NPS-PH-05-001, Naval Postgraduate School, Monterey, May 2005.

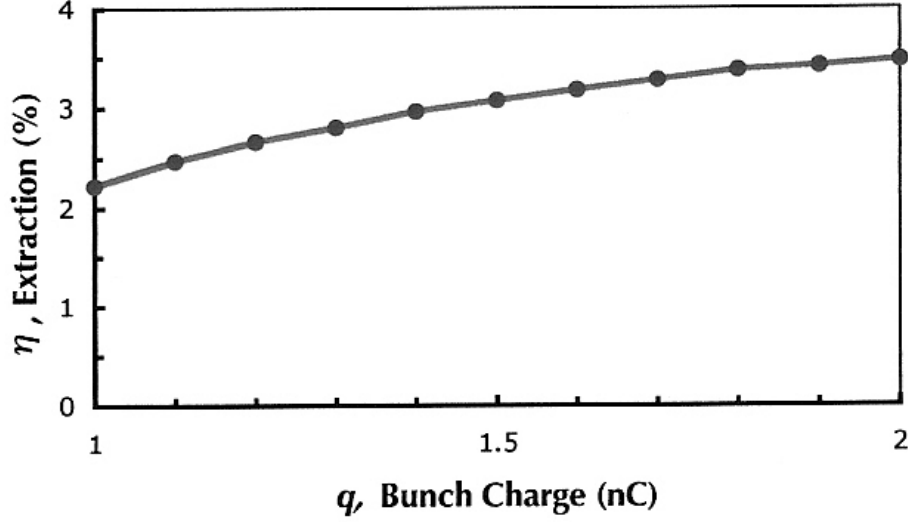


Figure 3.2: Plots of FEL performance as a function of individual design parameters, in this case bunch charge q , are each the result of many simulation runs.

Meanwhile, the dependence of *extraction* on number of undulator periods initially obeys (3.2), that is

$$\eta \propto \frac{1}{N}, \quad (3.8)$$

countering the trend due to increasing gain. In the high gain regime, extraction appears to have no dependence on N :

$$\begin{aligned} \eta &\approx \frac{\sqrt[3]{j/2}}{8N} \\ &\approx \frac{1}{8N} \sqrt[3]{\frac{4\pi^2 K^2 e^2 \lambda_0^2 N^3 n_e}{\gamma^3 mc^2}} \\ &\approx \sqrt[3]{\frac{\pi^2 K^2 e^2 \lambda_0^2 n_e}{128 \gamma^3 mc^2}}, \end{aligned} \quad (3.9)$$

and indeed the curve levels off once maximum gain is achieved, around $N = 15$ for this laser.

Figure 3.4 illustrates the effects of two important FEL concepts: filling factor F and (normalized) transverse emittance ε_n , given by

$$\varepsilon_n = \gamma r_b \theta_b, \quad (3.10)$$

where γ is the electron beam energy, r_b is the rms beam radius, and θ_b is its rms angular spread. In general, low emittance is desirable, and the value can only increase as the beam travels around the FEL transport lattice. Considerable pains are taken to suppress emittance

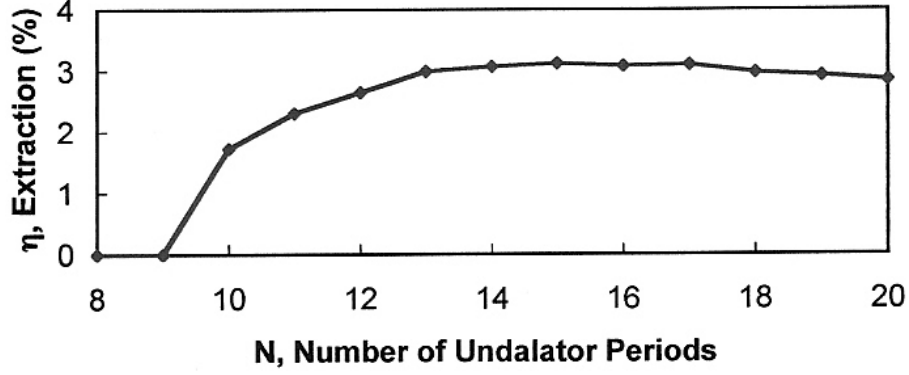


Figure 3.3: Plot of extraction η as a function of number of undulator periods N . While the curve is relatively flat beyond $N = 15$, a guiding principal in FEL design is using just enough undulator periods to get a working, efficient laser.

growth, but it is never zero, as evidenced when the electron beam is focused at the center of the undulator. Since ε_n must at least be conserved, the narrower the waist of the electron beam, the greater the angular spread. Too narrow a waist, and some electrons fall outside the optical mode at the ends of the undulator due to a large angular spread, as in the top of Figure 3.5. On the other hand, the electrons in a wider beam interact with a lower average optical field in the middle of the undulator, as in the bottom of the figure. Increasing F by increasing A_b may result in some electrons falling outside the optical mode, as illustrated in Figure 3.5. These electron still wiggle, but the radiation they produce is not reinforced by the optical resonator.

The important result from Figure 3.6 is that for a small increase in extraction achieved by increasing the Rayleigh length \tilde{z}_0 , there is a considerable increase in optical intensity on the resonator mirrors. This is of particular concern at present. Since vulnerability of the mirror limits the allowable power, material limitations make the value of mirror intensity a limiting factor in the development of weapon-class free electron lasers.

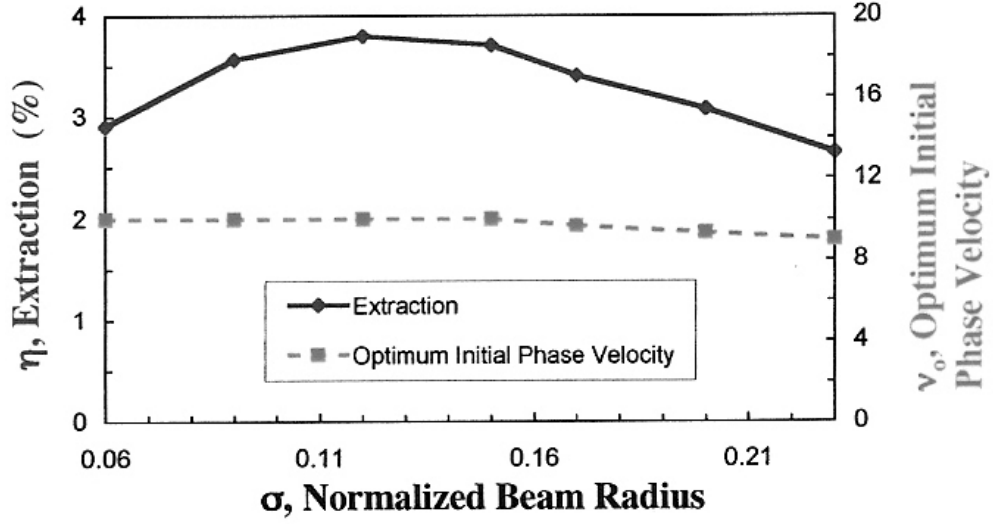


Figure 3.4: Plot of extraction η and optimum initial phase velocity ν_0 as a function of normalized electron beam waist radius σ for fixed transverse emittance ε_n . There is an optimum overlap between the electron beam and the optical mode.

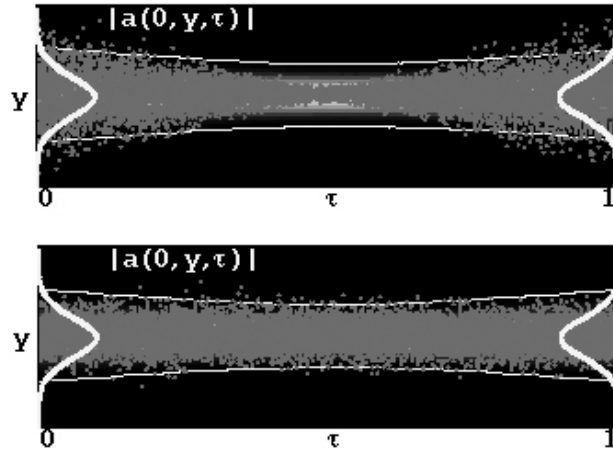


Figure 3.5: The overlap of the electron beam and the optical mode. A narrower electron beam means larger emittance ε_n and a lower number of interacting electrons, yet a wider beam creates an interaction region with a lower average optical field.

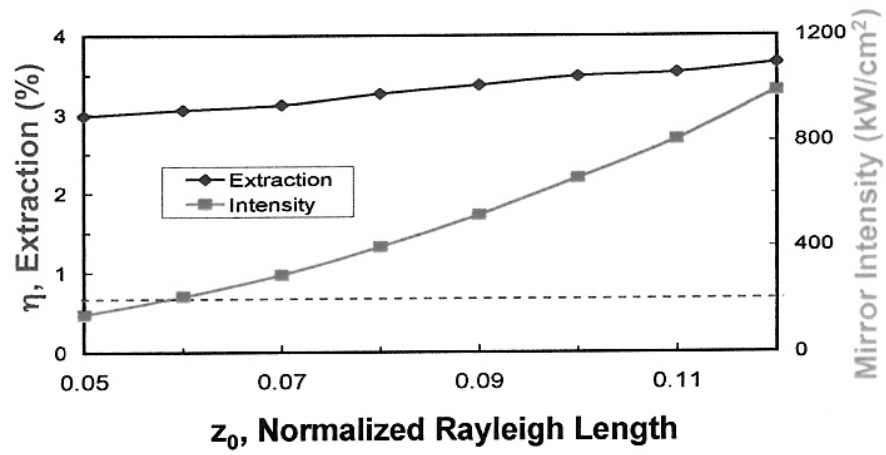


Figure 3.6: Plot of extraction η and mirror intensity as a function of normalized Rayleigh length \tilde{z}_0 . For longer Rayleigh lengths, a small increase in extraction is accompanied by a large increase in (potentially harmful) optical intensity on the resonator mirrors.

B. OPTICAL MODE DISTORTION

The simulation used in the 2003 runs was adequate to the task of determining the results described in the previous section: scientists at Thomas Jefferson National Accelerator Facility (JLAB), where the proposed laser was being developed, made use of the information provided, and the consideration of shorter Rayleigh length configurations was taken up as a serious endeavor.⁴

For the following year's runs, a number of improvements were made to the simulation code. A *faster* fast Fourier transform (FFT) algorithm⁵ was employed resulting in a 10-fold speed improvement. A more accurate propagation method involving *next*-nearest neighbors was utilized, and an expanding coordinate system that follows the rapidly diffracting wavefront made for greatly improved efficiency.

1. OPTICAL MODE DISTORTION IN A SHORT RAYLEIGH LENGTH FEL

A proposed high power FEL has the parameters shown in Table 3.1. As before, the simulation has the ability to follow multiple and arbitrary transverse optical modes, as they interact with the electron beam and bounce back and forth in the optical cavity, including mirror transmission and edge losses.⁶ Output from the improved simulation is shown in

Table 3.1: Parameters for a Proposed High-Power FEL

PARAMETER	SYMBOL	VALUE
electron beam energy	E_b	80 MeV
bunch charge	q	400 pC
bunch length	l_b	0.15 mm
peak current	\hat{I}	800 A
normalized emittance	ε_n	3 mm·mrad
beam radius	r_b	60 μm
undulator periods	N	22
undulator wavelength	λ_0	2.36 cm
undulator length	L	52 cm
peak magnetic field	\tilde{B}	0.7 T
undulator parameter	K	1
optical cavity length	S	18 m
Rayleigh length	z_0	6 cm
resonator quality factor	Q_n	4
optical wavelength	λ	1 μm

⁴At this writing, an experiment is in place at JLAB involving a resonator configuration utilizing a Rayleigh length on the order of $\tilde{z} = 0.2$.

⁵M. Frigo and S. G. Johnson, "FFTW: An Adaptive Software Architecture for the FFT", *Proceedings, 1998 International Conference on Acoustics and Signal Processing*, p. 1381, 1998.

⁶J. Blau, et al, "Optical Mode Distortion in a Short Rayleigh Length Free Electron Laser", *Proceedings, 26th International Free Electron Laser Conference*, Trieste, Italy, September, 2004.

2. RESULTS

When the wavefront pictures provided by the simulation were included in the plots of the parameters being varied to find optimum extraction (Figures 3.8 and 3.9), it became clear that *under certain configurations*,⁷ a FEL operates in higher-order modes. It is interest-

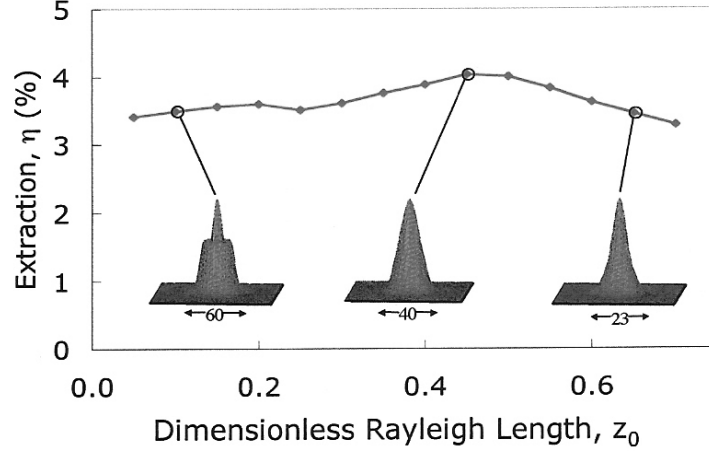


Figure 3.8: Plot of extraction η as a function of dimensionless Rayleigh length \tilde{z}_0 and wavefront pictures generated by the simulation.

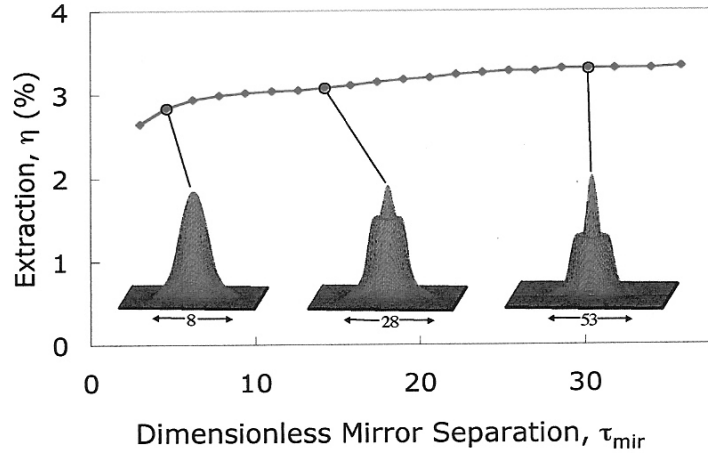


Figure 3.9: Plot of extraction η as a function of dimensionless mirror separation τ_{mir} and wavefront pictures generated by the simulation.

ing to note that while varying the Rayleigh length z_0 (Figure 3.8) and mirror separation τ_{mir} (Figure 3.9) evoke a relatively flat response from the FEL in terms of extraction, the new boundary conditions imposed by these changes appear to lead to a change in modal composition of the beam.

⁷For example, under certain Rayleigh lengths or distances between resonator mirrors. Remember that we said the FEL automatically finds the optimum ν_0 , so each data point in Figures 3.8 and 3.9 represents an operating FEL, with associated pictures indicating the shape of its optical wavefront.

C. THE NEED FOR HIGHER-ORDER MODE ANALYSIS

The radially symmetric, generally papilloid shape of the higher-order mode wavefronts observed in the 2003 and 2004 simulation results is suggestive of the geometry of the FEL resonator system and the boundary conditions imposed by an optical wave propagating along and around a coaxial column of current (see Figure 3.10, below). Under the assumption that

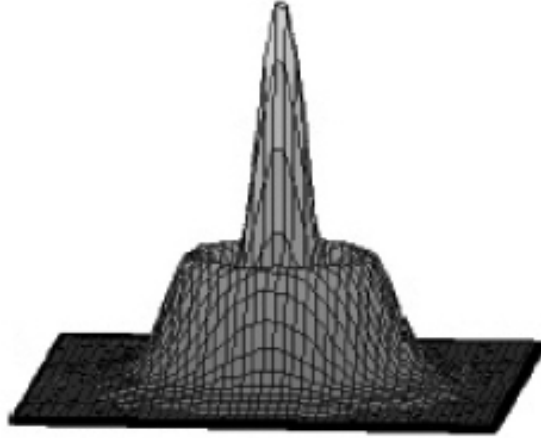


Figure 3.10: Wavefront suggesting coincident reinforcement of the optical mode by the electron beam. This is the general shape we see in many FEL simulations, which display the beam structure at the high reflector end of the resonator. The appearance of such structure demands a detailed analysis of the modal content of the outcoupled beam.

the fundamental Gaussian mode is the ideal mode both for lasing efficiency and atmospheric propagation, a simple index of beam quality⁸ would be sufficient. The observation from simulations that higher-order modes occur within the resonator demands a more robust characterization of beam quality. In other words, we wish to know more precisely which modes comprise our beam.

⁸One such measure of beam quality frequently encountered in the literature is M^2 , given by

$$M^2 = \left(\frac{d}{d_0} \right)^2,$$

where d is the observed beam diameter and

$$d_0 = 2\sqrt{\frac{z_0\lambda}{\pi}}$$

is the diameter of a theoretical diffraction-limited Gaussian beam arising from the same initial conditions. For more on M^2 see SAFNETT, and SIEGMAN 1993.

THIS PAGE INTENTIONALLY LEFT BLANK

CHAPTER IV.

HIGHER-ORDER MODES

An approach to the resolution of a given laser beam into its component modes is a process analogous to a Fourier decomposition of a function. In the same way that an arbitrary function¹ may be represented by a series of sines and/or cosines, *an arbitrary laser beam may be represented by a sum of orthogonal modes*. Identifying the appropriate complete, orthogonal basis set is the challenge, and is the topic of this chapter.

A. HERMITE-GAUSSIAN BEAMS

The trial solution we used to solve the parabolic wave equation in §1. can be further generalized to allow for higher-order modes. We begin by noting that (2.45) can be expressed as a product of identically dependent functions of each transverse coordinate, that is

$$\begin{aligned}
 \mathcal{E}(\tilde{x}, \tilde{y}, \tau) &= \mathcal{E}_0 \frac{\tilde{w}_0}{\tilde{w}} e^{-\tilde{r}^2/\tilde{w}^2} e^{i\tilde{r}^2\tau/(\tilde{z}_0^2+\tau^2)} e^{-i\arctan(\tau/\tilde{z}_0)} \\
 &= \mathcal{E}_0 \frac{\tilde{w}_0}{\tilde{w}} e^{-\tilde{x}^2/\tilde{w}^2} e^{-\tilde{y}^2/\tilde{w}^2} e^{i\tilde{x}^2\tau/(\tilde{z}_0^2+\tau^2)} e^{i\tilde{y}^2\tau/(\tilde{z}_0^2+\tau^2)} e^{-i\arctan(\tau/\tilde{z}_0)} \\
 &= \sqrt{\mathcal{E}_0 \frac{\tilde{w}_0}{\tilde{w}}} e^{-i\arctan(\tau/\tilde{z}_0)/2} e^{-\tilde{x}^2/\tilde{w}^2} e^{i\tilde{x}^2\tau/(\tilde{z}_0^2+\tau^2)} \times \\
 &\quad \sqrt{\mathcal{E}_0 \frac{\tilde{w}_0}{\tilde{w}}} e^{-i\arctan(\tau/\tilde{z}_0)/2} e^{-\tilde{y}^2/\tilde{w}^2} e^{i\tilde{y}^2\tau/(\tilde{z}_0^2+\tau^2)} \\
 &= \mathcal{E}_x(\tilde{x}, \tau) \mathcal{E}_y(\tilde{y}, \tau).
 \end{aligned} \tag{4.1}$$

As such, we can simplify the process of finding higher-order solutions by examining only one transverse dimension at a time. Writing the wave equation as

$$\left(-\frac{i}{4} \frac{\partial^2}{\partial \tilde{x}^2} + \frac{\partial}{\partial \tau} \right) \mathcal{E}_x = 0, \tag{4.2}$$

¹The function must, of course, meet the Dirichlet conditions: on any finite interval, it must possess one minimum, one maximum, and no discontinuities.

and modifying our trial solution to give the complex amplitude function p an explicit transverse dependence,

$$\mathcal{E}_x(\tilde{x}, \tau) = \mathcal{E}_0 p(\tilde{x}, \tau) e^{-\tilde{x}^2/q(\tau)}, \quad (4.3)$$

we begin taking derivatives:

$$\frac{\partial^2 \mathcal{E}}{\partial \tilde{x}^2} = \left[\frac{\partial^2 p}{\partial \tilde{x}^2} - \frac{4}{q} \tilde{x} \frac{\partial p}{\partial \tilde{x}} + \left(\frac{4}{q^2} \tilde{x}^2 - \frac{2}{q} \right) p \right] \mathcal{E}_0 e^{-\tilde{x}^2/q}, \quad (4.4)$$

$$\frac{\partial \mathcal{E}}{\partial \tau} = \left(\frac{\partial p}{\partial \tilde{x}} + \frac{1}{q^2} \frac{dq}{d\tau} \tilde{x}^2 p \right) \mathcal{E}_0 e^{-\tilde{x}^2/q}, \quad (4.5)$$

to give

$$\left(-\frac{i}{4} \frac{\partial^2 p}{\partial \tilde{x}^2} + \frac{i}{q} \tilde{x} \frac{\partial p}{\partial \tilde{x}} - \frac{i}{q^2} \tilde{x}^2 p + \frac{i}{2q} p + \frac{\partial p}{\partial \tau} + \frac{\tilde{x}^2}{q^2} \frac{dq}{d\tau} p \right) \mathcal{E}_0 e^{-\tilde{x}^2/q} = 0. \quad (4.6)$$

Dividing through by $-\frac{i}{4} \mathcal{E}_0 e^{-\tilde{x}^2/q}$ and collecting terms in spatial derivatives of p gives

$$\frac{\partial^2 p}{\partial \tilde{x}^2} - \frac{4}{q} \tilde{x} \frac{\partial p}{\partial \tilde{x}} + \left[\left(1 + i \frac{dq}{d\tau} \right) \frac{4}{q^2} \tilde{x}^2 - \frac{2}{q} \right] p + 4i \frac{\partial p}{\partial \tau} = 0. \quad (4.7)$$

It is the similarity of (4.7) to the well known Hermite differential equation

$$\frac{d^2 H_m}{du^2} - 2u \frac{dH_m}{du} + 2m H_m = 0 \quad (4.8)$$

that, after some algebra, leads to the following expression for the Hermite-Gaussian beam:²

$$\mathcal{E}(\tilde{x}, \tau) = \mathcal{E}_0 \frac{\tilde{w}_0}{\tilde{w}} H_m \left(\frac{\sqrt{2} \tilde{x}}{\tilde{w}} \right) e^{-\tilde{x}^2/\tilde{z}_0} e^{i\phi_{m0}(\tilde{x}, \tau)}, \quad (4.9)$$

or in three dimensions

$$\mathcal{E}(\tilde{x}, \tilde{y}, \tau) = \mathcal{E}_0 \frac{\tilde{w}_0}{\tilde{w}} H_m \left(\frac{\sqrt{2} \tilde{x}}{\tilde{w}} \right) H_n \left(\frac{\sqrt{2} \tilde{y}}{\tilde{w}} \right) e^{-\tilde{r}^2/\tilde{z}_0} e^{i\phi_{mn}(\tilde{r}, \tau)}, \quad (4.10)$$

where

$$\phi_{mn}(\tilde{r}, \tau) \equiv \frac{\tilde{r}^2 \tau}{\tilde{z}_0^2 + \tau^2} - (m + n + 1) \arctan \frac{\tau}{\tilde{z}_0}, \quad (4.11)$$

and H_m and H_n are m^{th} - and n^{th} -order solutions to (4.8). These so-called Hermite-Gaussian solutions to the dimensionless parabolic wave equation constitute a complete set of orthogonal modes with which one may construct an arbitrary laser beam wavefront.

The properties of Hermite polynomials are well documented.³ The first ten polynomials are listed in Table 4.1. Some examples of the effect of the functions H_m and H_n on the beam wavefront is represented in Figure 4.1. These “burn patterns” illustrate the *intensity* \mathcal{E}^2 of the beam in the transverse plane, but display nothing about the phase! To fully characterize a beam, one must know both its amplitude and phase at every point, a challenge in a real experiment, but a matter of course in a simulation.

²The (dimensional) functional forms of $\mathcal{E}(\tilde{x}, \tilde{y}, \tau)$ as well as a derivation of the higher-order solution are available in A. E. Siegman, *Lasers*, University Science Books, Sausalito, 1986. We include the dimensionless forms of the τ -dependent expressions for completeness.

³See, for example, pp. 367-9, V. Barcion, “Special Functions” in C. E. Pearson, Ed., *Handbook of Applied Mathematics*, Van Nostrand Reinhold, New York, 1983.

Table 4.1: Hermite Polynomials - Solutions to $\frac{d^2 H_m}{du^2} - 2u \frac{dH_m}{du} + 2mH_m = 0$

$H_0(u)$	=	1
$H_1(u)$	=	$2u$
$H_2(u)$	=	$4u^2 - 2$
$H_3(u)$	=	$8u^3 - 12u$
$H_4(u)$	=	$16u^4 - 48u^2 + 12$
$H_5(u)$	=	$32u^5 - 160u^3 + 120u$
$H_6(u)$	=	$64u^6 - 480u^4 + 720u^2 - 120$
$H_7(u)$	=	$128u^7 - 1344u^5 + 3360u^3 - 1680u$
$H_8(u)$	=	$256u^8 - 3584u^6 + 13440u^4 - 13440u^2 + 1680$
$H_9(u)$	=	$512u^9 - 9216u^7 + 48384u^5 - 80640u^3 + 30240u$

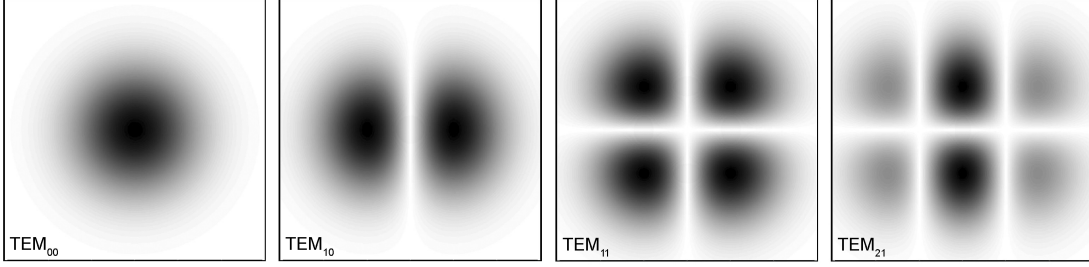


Figure 4.1: Some Hermite-Gaussian modes. The transverse electromagnetic (TEM) subscripts correspond to the values of m and n in the polynomials H_m and H_n .

B. LAGUERRE-GAUSSIAN BEAMS

In cylindrical coordinates, the dimensionless transverse Laplacian is

$$\nabla_{\perp}^2 \equiv \frac{1}{\tilde{r}} \frac{\partial}{\partial \tilde{r}} \left(\tilde{r} \frac{\partial}{\partial \tilde{r}} \right) + \frac{1}{\tilde{r}^2} \frac{\partial^2}{\partial \tilde{\theta}^2}, \quad (4.12)$$

and (2.17) becomes

$$\frac{1}{\tilde{r}} \frac{\partial \mathcal{E}}{\partial \tilde{r}} \left(\tilde{r} \frac{\partial \mathcal{E}}{\partial \tilde{r}} \right) + \frac{1}{\tilde{r}^2} \frac{\partial^2 \mathcal{E}}{\partial \tilde{\theta}^2} + \frac{\partial \mathcal{E}}{\partial \tau} = 0. \quad (4.13)$$

We might guess that this coordinate system is more appropriate to the resonator geometry, whose eigenmodes are certain to reflect the circular shape of the mirrors. Following the same procedure as in the previous section, a generalized trial solution to (4.12) yields a differential equation similar to Laguerre's differential equation

$$u \frac{d^2 L_p}{du^2} + (m+1-r) \frac{dL_p}{du} + pL_p = 0. \quad (4.14)$$

Like the Hermite polynomials, the polynomials that solve (4.14) also constitute a complete set of orthogonal functions, the first ten of which are given in Table 4.2.

Table 4.2: Laguerre Polynomials - Solutions to $u \frac{d^2 L_p}{du^2} + (1-u) \frac{dL_p}{du} + pL_p = 0$

$L_0(u)$	=	1
$L_1(u)$	=	$1 - u$
$L_2(u)$	=	$1 - 2u + \frac{1}{2}u^2$
$L_3(u)$	=	$1 - 3u + \frac{3}{2}u^2 - \frac{1}{6}u^3$
$L_4(u)$	=	$1 - 4u + 3u^2 - \frac{2}{3}u^3 + \frac{1}{24}u^4$
$L_5(u)$	=	$1 - 5u + 5u^2 - \frac{5}{3}u^3 + \frac{5}{24}u^4 - \frac{1}{120}u^5$
$L_6(u)$	=	$1 - 6u + \frac{15}{2}u^2 - \frac{10}{3}u^3 + \frac{5}{8}u^4 - \frac{1}{20}u^5 + \frac{1}{720}u^6$
$L_7(u)$	=	$1 - 7u + \frac{21}{2}u^2 - \frac{35}{6}u^3 + \frac{35}{24}u^4 - \frac{7}{40}u^5 + \frac{7}{720}u^6 - \frac{1}{5040}u^7$
$L_8(u)$	=	$1 - 8u + 14u^2 - \frac{28}{3}u^3 + \frac{35}{12}u^4 - \frac{7}{15}u^5 + \frac{7}{180}u^6 - \frac{1}{630}u^7 + \frac{1}{40320}u^8$
$L_9(u)$	=	$1 - 9u + 18u^2 - 14u^3 + \frac{21}{4}u^4 - \frac{21}{20}u^5 + \frac{7}{60}u^6 - \frac{1}{140}u^7 + \frac{1}{4480}u^8 - \frac{1}{362880}u^9$

The Laguerre-Gaussian beam, given by

$$\mathcal{E}(\tilde{r}, \theta, \tau) = \mathcal{E}_0 \frac{\tilde{w}_0}{\tilde{w}} \left(\frac{\sqrt{2}\tilde{r}}{\tilde{w}} \right)^m L_p^m \left(\frac{2\tilde{r}^2}{\tilde{w}^2} \right) e^{-\tilde{r}^2/\tilde{w}^2} e^{i\phi_p^m(\tilde{r}, \theta, \tau)}, \quad (4.15)$$

where

$$\phi_p^m(\tilde{r}, \theta, \tau) \equiv \frac{\tilde{r}^2 \tau}{\tilde{z}_0^2 + \tau^2} - (2p + m + 1) \arctan \frac{\tau}{\tilde{z}_0} + m\theta, \quad (4.16)$$

is a dimensionless solution to the parabolic wave equation in cylindrical coordinates.⁴ Beam propagation is shown for the first ten Laguerre-Gaussian modes in Figure 4.2. Evidently, the wavefronts retain their shape. Examining (4.15), we see there is no change in the number of zeros as τ increases: there is no “crossing” of local maxima.

⁴The subscripts m and n are standard in the literature for the Hermite polynomials. Similarly, m and p are often used for the Laguerre indices. At this point, we essentially leave behind our discussion of Hermite-Gaussian beams, so from now on m will denote the angular mode of the Laguerre-Gaussian solution.

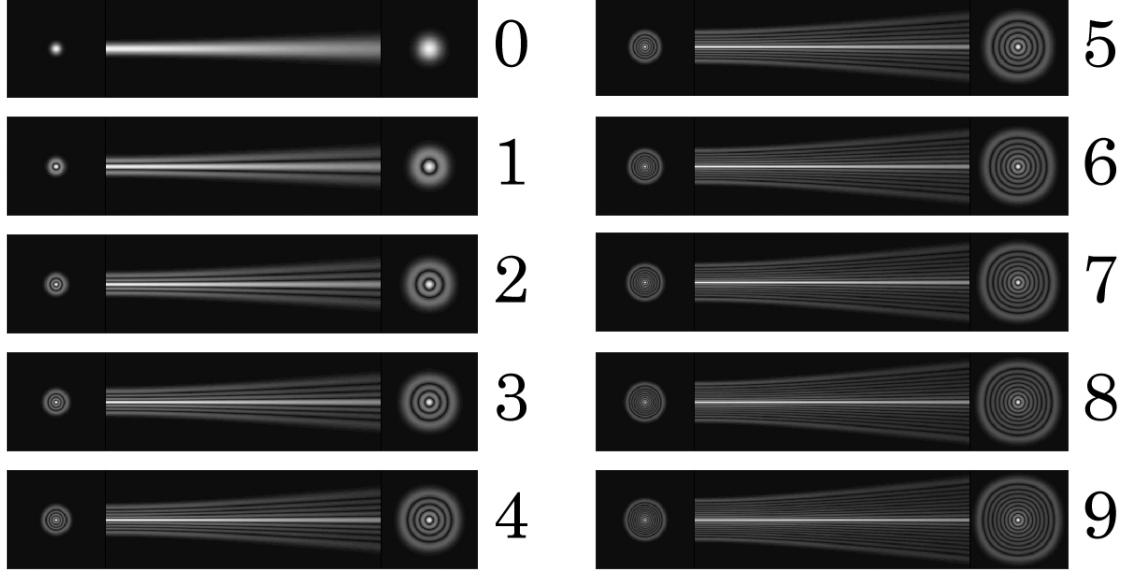


Figure 4.2: The first ten Laguerre-Gaussian modes. Notice that L_0^0 is simply a Gaussian beam. Notice also that all modes retain their general shape—in particular the number of zeros—as they propagate through a sourceless medium.

The orthogonality of the generalized Laguerre polynomials is weighted by $u^m e^{-u}$ with the normalization⁵

$$\int_0^\infty u^m e^{-u} L_p^m(u) L_q^m(u) du = \frac{\Gamma(q+m+1)}{q!} \delta_{pq}, \quad (4.17)$$

where

$$\Gamma(\alpha) = \int_0^\infty e^{-u} u^{\alpha-1} du. \quad (4.18)$$

We shall only consider those Laguerre modes with no azimuthal dependence, that is $m = 0$. For integers (which $q + 1$ surely is)

$$\Gamma(n) = (n-1)!, \quad (4.19)$$

and so, for our purposes, we shall write the orthogonality condition as

$$\int_0^\infty e^{-u} L_p(u) L_q(u) du = \delta_{pq}. \quad (4.20)$$

Now, finding the Laguerre-Gaussian (LG) “spectrum” of an arbitrary initial wavefront $E(\tilde{r}, 0)$ with azimuthal symmetry requires us to calculate the coefficients c_p in the series

$$E(\tilde{r}, 0) = \sum_p c_p \mathcal{E}_p(\tilde{r}, 0) \quad (4.21)$$

⁵See pp. 533-4 in D. Zwillinger, *CRC Standard Mathematical Tables and Formulae*, Chapman & Hall, New York, 2003.

where

$$\mathcal{E}_p(\tilde{r}, 0) = \mathcal{E}_0 L_p \left(\frac{2\tilde{r}^2}{\tilde{z}_0} \right) e^{-\tilde{r}^2/\tilde{z}_0} \quad (4.22)$$

solves (4.13) at $\tau = 0$. Notice that the factor $e^{i\phi_p^m(\tilde{r}, \theta, \tau)}$ in (4.15) becomes unity since

$$\begin{aligned} \phi_p^0(\tilde{r}, 0, 0) &= \frac{\tilde{r}^2 \times 0}{\tilde{z}_0^2 + 0} - (2p + 0 + 1) \arctan \frac{0}{\tilde{z}_0} + 0 \times 0 \\ &= 0. \end{aligned} \quad (4.23)$$

Expressing our arbitrary wavefront as a function of

$$\varrho = \frac{2\tilde{r}^2}{\tilde{w}^2} \quad (4.24)$$

and noting that⁶

$$\varrho_0 = \frac{2\tilde{r}^2}{\tilde{w}_0^2} = \frac{2\tilde{r}^2}{\tilde{z}_0}, \quad (4.25)$$

we multiply both sides of (4.21) by an LG mode $\mathcal{E}_q(\varrho_0)$ and integrate over ϱ_0 :

$$\begin{aligned} \int_0^\infty E(\varrho_0) \mathcal{E}_q(\varrho_0) d\varrho_0 &= \int_0^\infty \sum_p c_p \mathcal{E}_p(\varrho_0) \mathcal{E}_q(\varrho_0) d\varrho_0 \\ &= \mathcal{E}_0^2 \sum_p c_p \int_0^\infty e^{-\varrho_0} L_p(\varrho_0) L_q(\varrho_0) d\varrho_0 \\ &= \mathcal{E}_0^2 \sum_p c_p \delta_{pq} \\ &= \mathcal{E}_0^2 c_q, \end{aligned} \quad (4.26)$$

⁶For example, using this new coordinate the Gaussian beam becomes

$$\mathcal{E}_0 e^{-\tilde{r}^2/\tilde{z}_0} \rightarrow \mathcal{E}_0 e^{-\varrho_0/2}.$$

where we have used (4.20). An arbitrary coefficient is then⁷

$$\begin{aligned} c_q &= \frac{1}{\mathcal{E}_0^2} \int_0^\infty E(\varrho_0) \mathcal{E}_q(\varrho_0) d\varrho_0 \\ &= \frac{4}{\mathcal{E}_0 \tilde{z}_0} \int_0^\infty \tilde{r} e^{-\tilde{r}^2/\tilde{z}_0} L_q\left(\frac{2\tilde{r}^2}{\tilde{z}_0}\right) E(\tilde{r}) d\tilde{r}. \end{aligned} \quad (4.27)$$

Equation (4.27) is limited to $\tau = 0$. Even as we assert the usefulness of a modal analysis of the initial wavefront, we wish to analyze our beam at any point along its propagation, that is for any τ . Beginning once again with (4.21), this time we make no assumptions about the value of τ and thus $\tilde{w}(\tau)$ and the τ -dependent phase factor $e^{i\phi_p^m(\tilde{r}, \theta, \tau)}$:

$$E(\varrho, \tau) = \sum_p c_p \mathcal{E}_p(\varrho, \tau) \quad (4.28)$$

Implicit in this generalization is the possibility of a complex $c_p(\tau)$. Here is why. Suppressing the arguments ϱ and τ , let us multiply both sides of (4.28) by arbitrary mode \mathcal{E}_q^* and

⁷We can normalize the quantity $\sum_p c_p$ to unity by setting $E(\tilde{r})$ to the fundamental and calculating

$$\begin{aligned} c_0 &= \frac{4}{\mathcal{E}_0 \tilde{z}_0} \int_0^\infty \tilde{r} e^{-\tilde{r}^2/\tilde{z}_0} e^{-\tilde{r}^2/\tilde{z}_0} d\tilde{r} \\ &= \frac{4}{\mathcal{E}_0 \tilde{z}_0} \int_0^\infty \tilde{r} e^{-2\tilde{r}^2/\tilde{z}_0} d\tilde{r} \\ &= \frac{4}{\mathcal{E}_0 \tilde{z}_0} \times \frac{\tilde{z}_0}{4} \\ &= \frac{1}{\mathcal{E}_0}, \end{aligned}$$

where we have used

$$\int_0^\infty x^n e^{-ax^p} dx = \frac{\Gamma[(n+1)/p]}{pa^{(n+1)/p}},$$

with $n = 1$, $a = 2/\tilde{z}_0$, and $p = 2$ (see p. 451, ZWILLINGER). Having thus identified

$$\frac{1}{\mathcal{E}_0} = 1,$$

and returning to our standard LG index p , a normalized Laguerre-Gaussian spectral coefficient is then

$$\hat{c}_p = \int_0^\infty e^{-\tilde{r}^2/\tilde{z}_0} L_p\left(\frac{2\tilde{r}^2}{\tilde{z}_0}\right) E(\tilde{r}) d\tilde{r},$$

with the carat indicating normalization. While this is a useful result, we ultimately intend to approach the calculation of LG-spectrum coefficients numerically, and a self-consistent normalization will be included in the computer program. The above is included for completeness.

integrate:

$$\begin{aligned}
\int_0^\infty E \mathcal{E}_q^* d\varrho &= \int_0^\infty \sum_p c_p \mathcal{E}_p \mathcal{E}_q^* d\varrho \\
&= \mathcal{E}_0^2 \sum_p c_p \int_0^\infty e^{i(\phi_p - \phi_q)} e^{-\varrho} L_p(\varrho) L_q(\varrho) d\varrho \\
&= \mathcal{E}_0^2 \sum_p c_p e^{2i(p-q) \arctan(\tau/\tilde{z}_0)} \int_0^\infty e^{-\varrho} L_p(\varrho) L_q(\varrho) d\varrho \\
&= \mathcal{E}_0^2 \sum_p c_p e^{2i(p-q) \arctan(\tau/\tilde{z}_0)} \delta_{pq} \\
&= \mathcal{E}_0^2 c_q,
\end{aligned} \tag{4.29}$$

and so, switching indices from q to our standard p ,

$$c_p = \frac{1}{\mathcal{E}_0^2} \int_0^\infty E \mathcal{E}_p^* d\varrho \tag{4.30}$$

or explicitly

$$\begin{aligned}
c_p &= \frac{\tilde{w}_0}{\mathcal{E}_0 \tilde{w}} e^{i(2p+1) \arctan(\tau/\tilde{z}_0)} \int_0^\infty e^{-\mathfrak{z}\varrho/2} L_p(\varrho) E(\varrho, \tau) d\varrho \\
&= \frac{4\tilde{z}_0}{\mathcal{E}_0 \tilde{w}} e^{i(2p+1) \arctan(\tau/\tilde{z}_0)} \int_0^\infty \tilde{r} e^{-\mathfrak{z}\tilde{r}^2/\tilde{w}^2} L_p\left(\frac{2\tilde{r}^2}{\tilde{w}^2}\right) E(\tilde{r}, \tau) d\tilde{r},
\end{aligned} \tag{4.31}$$

where once again

$$\mathfrak{z} = 1 + i \frac{\tau}{\tilde{z}_0}. \tag{4.32}$$

We will attempt to solve (4.31) numerically, for two reasons: (1) while we may know the amplitude and phase of a simulated FEL beam at every (finite) transverse point, we will not generally have an analytic expression for the entire wavefront; and (2) even if we did know the functional form of $E(\tilde{r}, \tau)$, the integral in (4.31) is difficult to perform for all but the most ideal beams.

For a numerical analysis, we must first get the integral into a form the computer can understand. Letting the subscripts r and i indicate the real and imaginary parts, we rewrite (4.30) as

$$\begin{aligned}
c_p &= \frac{1}{\mathcal{E}_0^2} \int_0^\infty \mathcal{E}_p^* E d\varrho \\
&= \frac{1}{\mathcal{E}_0^2} \int_0^\infty (\mathcal{E}_{p,r} - i\mathcal{E}_{p,i}) (E_r + iE_i) d\varrho \\
&= \frac{1}{\mathcal{E}_0^2} \int_0^\infty (\mathcal{E}_{p,r} E_r + i\mathcal{E}_{p,r} E_i - i\mathcal{E}_{p,i} E_r + \mathcal{E}_{p,i} E_i) d\varrho \\
&= \frac{1}{\mathcal{E}_0^2} \int_0^\infty (\mathcal{E}_{p,r} E_r + \mathcal{E}_{p,i} E_i) d\varrho + \frac{i}{\mathcal{E}_0^2} \int_0^\infty (\mathcal{E}_{p,r} E_i - \mathcal{E}_{p,i} E_r) d\varrho
\end{aligned} \tag{4.33}$$

We may now split c_p into its real and imaginary parts, each of which may be integrated separately:

$$c_{p,r} \equiv \Re\{c_p\} = \frac{1}{\mathcal{E}_0^2} \int_0^\infty (\mathcal{E}_{p,r} E_r + \mathcal{E}_{p,i} E_i) d\rho, \quad (4.34a)$$

$$c_{p,i} \equiv \Im\{c_p\} = \frac{1}{\mathcal{E}_0^2} \int_0^\infty (\mathcal{E}_{p,r} E_i - \mathcal{E}_{p,i} E_r) d\rho. \quad (4.34b)$$

The contribution to the LG spectrum of an arbitrary beam by an individual LG mode shall be given by the modulus of that mode's coefficient,

$$c_p = |c_p| = \sqrt{c_{p,r}^2 + c_{p,i}^2}, \quad (4.35)$$

and will be normalized to the sum of all basis set coefficients:

$$\hat{c}_p = \frac{c_p}{\sum_q c_q}. \quad (4.36)$$

C. NUMERICAL PROPAGATION OF HIGHER-ORDER MODES

The diagnostic tool to be included in free electron laser simulations numerically integrates (4.34) and reports c_p for each of the first ten LG modes via (4.35). Figure 4.3 is a sample output from **bm.c**, a self-contained code that resolves an input laser beam wavefront into component LG modes and reports the normalized LG coefficients as a bar chart beneath the wavefront picture both before and after propagation. In this case, the integration has correctly identified the initial wavefront as an exclusively LG-2 beam: in the bar chart below the initial wavefront intensity plot, only the bar in the third position is present and goes to the top of the chart. To within a few percent error, the program has also determined the final wavefront to be LG-2, as we expect. The text in the middle of the output reports parameters used for that simulation as well as a “fractional energy on target” for a circular target of fixed radius. This is discussed in the next section. The basis sets used to analyze the input beam both before and after propagation are evaluated analytically and displayed at the bottom of the output for reference.

The diagnostic is able to pick out multiple modes, as in Figure 4.4. In this case, we see for the first time the “crossing” of zeros in the propagation of the laser beam. Remember that “pure” LG modes do not exhibit this behavior: a given Laguerre-Gaussian mode possesses the same number of zeros throughout its propagation (see again Figure 4.2). Single modes also always exhibit a global maximum at $\tilde{r} = 0$, not always observed in mixed modes. This distinction between single- and mixed-mode higher-order beams immediately suggests a useful application for our tool, and it leads us to consider one of the difficulties in the experimental analysis of laser beam modes.

It is not possible to determine the modal composition of a beam (function) if only its intensity (square) is known. As a simple illustration, let us consider the curves in Figure 4.5. It is not possible to determine whether the curve on the right was arrived at by squaring the

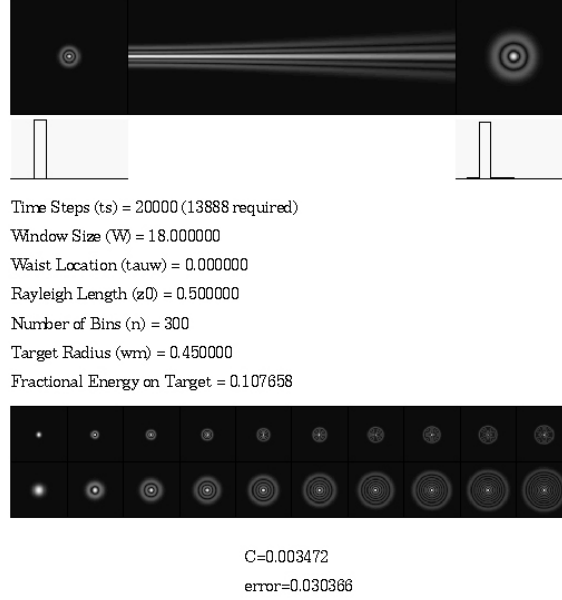


Figure 4.3: Output from the diagnostic tool **bm.c**. The basis set before and after propagation (evaluated analytically) is included at the bottom of the display for reference.

top left or bottom left function. An attempt to determine the modal composition of a laser beam based on intensity information alone encounters the same problem. It is precisely the phase information that is lost in the process of squaring.

Consequently, burn patterns can be misleading. Figure 4.6 shows the propagation of the same laser beam as Figure 4.4, but takes the cross sectional amplitude (or burn pattern) of the final wavefront earlier than before. Visually inspecting the initial and final wavefront amplitude plots (enlarged in Figure 4.7), one might be hard-pressed to conclude (or even guess!) that they were generated by the same laser beam. Yet the values of the LG coefficients, as reported in the bar charts beneath the initial and final wavefronts in Figure 4.6, assure us that this is the case. Multiple modes interfere because each mode prescribes a unique time dependence via the factor

$$e^{i\phi_p(\tilde{r},\tau)} \equiv \exp \left[i \frac{\tilde{r}^2 \tau}{\tilde{z}_0^2 + \tau^2} - i(2p+1) \arctan \frac{\tau}{\tilde{z}_0} \right] \quad (4.37)$$

in (4.15). This evolving phase-front results in an evolving amplitude-front as modes cyclically cancel and reinforce each other, as evident in the propagation plot.

The diagnostic tool performs well for even more complicated mixtures of higher-order Laguerre-Gaussian modes. In Figure 4.8, **bm.c** has correctly identified the 3:5:2 mixture of the LG-0, -3, and -6 modes comprising the simulated beam. Figure 4.9 shows the analysis of a beam comprised of many LG modes. Once again, in both figures we observe the zero crossings typical of mixed-mode beams, and the difference in the burn patterns before and after propagation.



Figure 4.4: A beam composed of two distinct Laguerre-Gaussian modes. The slight error in the bar chart pertaining to the LG coefficients for the final wavefront is a result of numerical integration error.

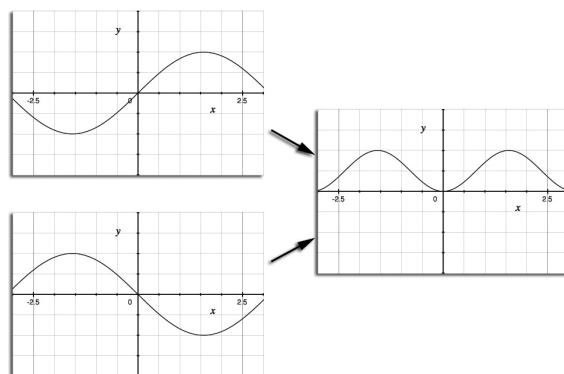


Figure 4.5: When squared, the two functions $\sin x$ (top left) and $\sin(x + \pi)$ (bottom left) lead to an identical squared function (right).

D. POWER ON TARGET

Knowing which modes comprise our laser beam allows us to examine the relationship between physical properties of the beam and its composition. An example of this is the important consideration of power on target: how much of the beam’s initial energy is focused onto a target at the propagation distance.

Choosing a circular target of an arbitrary radius such that almost all (93.5%) of the outcoupled energy is delivered to its surface when the beam is in the fundamental, Figure 4.10 plots the energy delivered to the same target by beams in unmixed, higher-order Laguerre-Gaussian modes.

Evidently, by themselves higher-order modes are not good choices for delivering power to a target at the center of the beam. As p increases, more and more energy is relegated to the “shoulders” of the central field (see Figure 4.11). Once in this outer region, light cannot cross back into the center without a change in the number of local field maxima—not observed in pure LG beams.

Certainly, real lasers are unlikely to be comprised solely of single higher-order Laguerre-Gaussian modes, or even predictable mixtures. Figure 4.12 shows three theoretical lasers: one a Gaussian, one an even mixture of the Gaussian and LG-1 modes, and one a beam with



Figure 4.6: Each LG mode carries a different phase factor, causing periodic interference when multiple modes are combined.

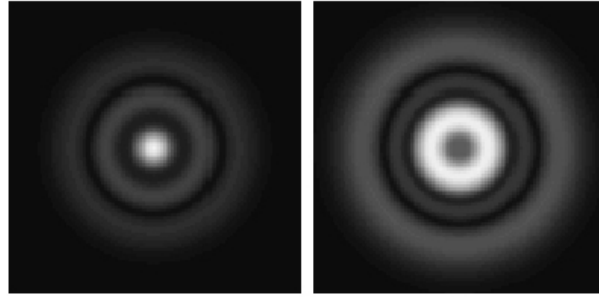


Figure 4.7: A combination of LG modes before (left) and after (right) propagation over a finite distance (enlarged from Figure 4.6). While the two wavefronts are not necessarily identifiable by eye as manifestations of the same laser beam, the diagnostic assures us this is so.

a “flat-top” cross section. The percentage of energy received by the centrally located target is shown.

What the propagation of mixed modes such as the flat-top beam teaches us is that the inclusion of higher-order in the laser does not necessarily spell doom for the propagation of power to the target area. Certainly the trend in Figure 4.10 is not towards larger central field amplitude for higher values of p . But mixed modes, as Figures 4.6, 4.8, and 4.9 demonstrate, have the potential to get some of that power from the shoulders back into the center of the beam. In fact, we may conclude that *any non-fundamental beam delivering more power to our test target than the L_1 -Gaussian is by definition comprised of multiple higher-order modes*. Particularly for use as a weapon, if a laser beam is not in the fundamental, it may benefit from the mixing of higher-order modes.

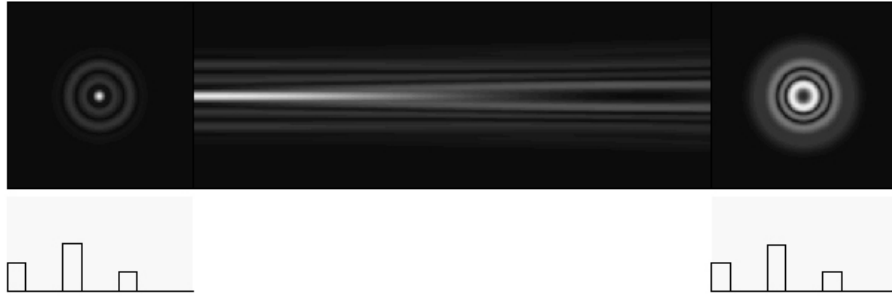


Figure 4.8: A beam comprised of three higher-order modes. The recipe is three parts LG-0 (the fundamental Gaussian), five parts LG-3, and two parts LG-6. Once again, the burn patterns before and after propagation are difficult to reconcile visually.

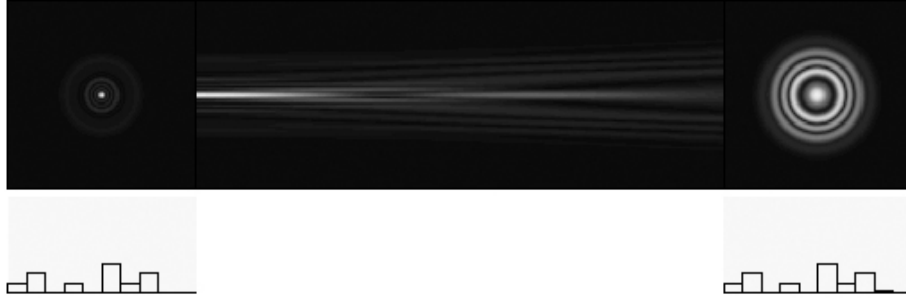


Figure 4.9: A beam comprised of many higher-order modes.

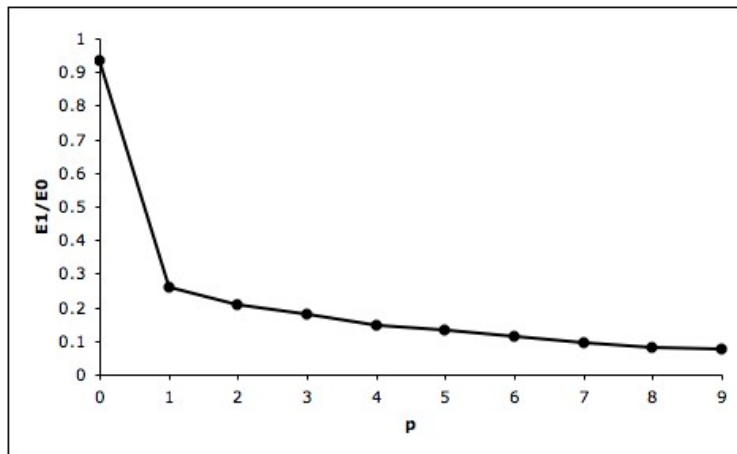


Figure 4.10: $E0$ and $E1$ are the energy contained in the beam and the energy delivered to the target area, respectively. For unmixed Laguerre-Gaussian modes, laser power on target drops off significantly for $p > 0$.

Energy in the “shoulder” falls outside the target area.

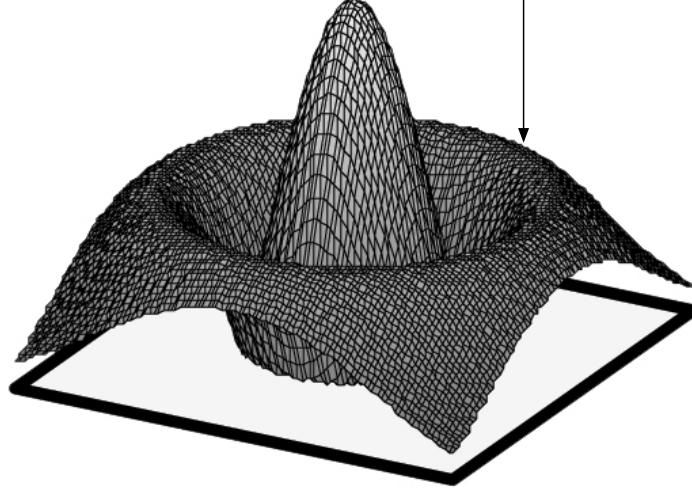


Figure 4.11: A target just large enough to receive nearly 100% of the energy in the fundamental will generally not receive energy from pure higher-order modes beyond the first zero-point.

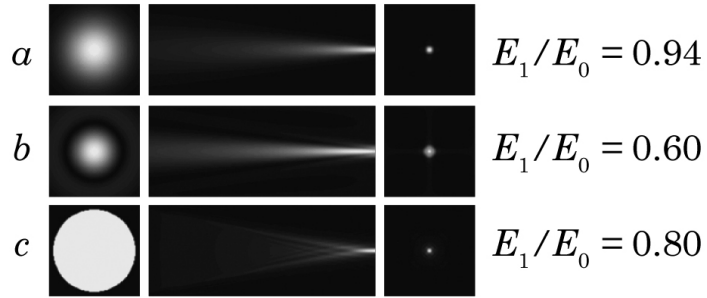


Figure 4.12: The propagation of (a) a Gaussian beam; (b) a beam comprised of equal parts L_0 - and L_1 -Gaussian modes; (c) an initially “flat-top” beam, defined by a step function at $\tilde{r} = \tilde{w}_0$ as determined by the fundamental Gaussian in (a). Notice once again the crossing of local maxima in (c), not observed for unmixed Laguerre-Gaussian modes. It is this crossing that has allowed the beam to deliver more energy to the center of the target.

E. CONCLUSION

Resolving arbitrary optical modes into higher-order mode spectra provides a useful tool for the analysis of FEL simulations and a self-consistent index of beam quality. Future work might include retaining the azimuthal index m in

$$\mathcal{E}(\tilde{r}, \theta, \tau) = \mathcal{E}_0 \frac{\tilde{w}_0}{\tilde{w}} \left(\frac{\sqrt{2}\tilde{r}}{\tilde{w}} \right)^m L_p^m \left(\frac{2\tilde{r}^2}{\tilde{w}^2} \right) e^{-\tilde{r}^2/\tilde{w}^2} e^{i\phi_p^m(\tilde{r}, \theta, \tau)},$$

where

$$\phi_p^m(\tilde{r}, \theta, \tau) \equiv \frac{\tilde{r}^2 \tau}{\tilde{z}_0^2 + \tau^2} - (2p + m + 1) \arctan \frac{\tau}{\tilde{z}_0} + m\theta,$$

during the analysis—such a basis set would be capable of generating *any* beam, even those without radial symmetry. Free electron laser simulations have also demonstrated the potential usefulness of the Hermite-Gaussian modes as an appropriate basis set when studying off-axis electron beams and/or resonator cavity mirror-tilt.

THIS PAGE INTENTIONALLY LEFT BLANK

APPENDIX: THE PARABOLIC WAVE EQUATION

We present the parabolic wave equation in both dimensionless and dimensional form.

Cartesian coordinates.

The dimensionless parabolic wave equation is

$$\frac{\partial \mathcal{E}}{\partial \tau} = \frac{i}{4} \nabla_{\perp}^2 \mathcal{E},$$

where

$$\begin{aligned} \tau &= \frac{z}{L}, \\ \nabla_{\perp}^2 &\equiv \frac{\partial^2}{\partial \tilde{x}^2} + \frac{\partial^2}{\partial \tilde{y}^2}, \end{aligned}$$

for a propagation distance L . Using the dimensionless coordinates

$$\tilde{x} \equiv \sqrt{\frac{\pi}{L\lambda}} x,$$

we can transform to the dimensional paraxial wave equation as follows:

$$\begin{aligned} L \frac{\partial \mathcal{E}}{\partial z} &= \frac{i}{4} \left(\frac{\partial^2 \mathcal{E}}{\partial \tilde{x}^2} + \frac{\partial^2 \mathcal{E}}{\partial \tilde{y}^2} \right), \\ \mathcal{L} \frac{\partial \mathcal{E}}{\partial z} &= \frac{i\mathcal{L}\lambda}{4\pi} \left(\frac{\partial^2 \mathcal{E}}{\partial x^2} + \frac{\partial^2 \mathcal{E}}{\partial y^2} \right), \\ \frac{\partial \mathcal{E}}{\partial z} &= \frac{i}{2k} \left(\frac{\partial^2 \mathcal{E}}{\partial x^2} + \frac{\partial^2 \mathcal{E}}{\partial y^2} \right), \end{aligned}$$

and finally the familiar

$$\frac{\partial^2 \mathcal{E}}{\partial x^2} + \frac{\partial^2 \mathcal{E}}{\partial y^2} + 2ik \frac{\partial \mathcal{E}}{\partial z} = 0.$$

Cylindrical coordinates.

In cylindrical coordinates we use

$$\nabla_{\perp}^2 \equiv \frac{1}{\tilde{r}} \frac{\partial}{\partial \tilde{r}} \left(\tilde{r} \frac{\partial}{\partial \tilde{r}} \right) + \frac{1}{\tilde{r}^2} \frac{\partial^2}{\partial \tilde{\theta}^2},$$

where $\tilde{r} \equiv r/w_L$ and $\tilde{\theta} = \theta$, and we have

$$\begin{aligned} L \frac{\partial \mathcal{E}}{\partial z} &= \frac{i}{4} \left[\frac{1}{\tilde{r}} \frac{\partial}{\partial \tilde{r}} \left(\tilde{r} \frac{\partial \mathcal{E}}{\partial \tilde{r}} \right) + \frac{1}{\tilde{r}^2} \frac{\partial^2 \mathcal{E}}{\partial \tilde{\theta}^2} \right], \\ \mathcal{L} \frac{\partial \mathcal{E}}{\partial z} &= \frac{i\mathcal{L}\lambda}{4\pi} \left[\frac{1}{r} \frac{\partial}{\partial r} \left(r \frac{\partial \mathcal{E}}{\partial r} \right) + \frac{1}{r^2} \frac{\partial^2 \mathcal{E}}{\partial \theta^2} \right], \\ \frac{\partial \mathcal{E}}{\partial z} &= \frac{i}{2k} \left[\frac{1}{r} \frac{\partial}{\partial r} \left(r \frac{\partial \mathcal{E}}{\partial r} \right) + \frac{1}{r^2} \frac{\partial^2 \mathcal{E}}{\partial \theta^2} \right], \end{aligned}$$

and finally

$$\frac{1}{r} \frac{\partial \mathcal{E}}{\partial r} \left(r \frac{\partial \mathcal{E}}{\partial r} \right) + \frac{1}{r^2} \frac{\partial^2 \mathcal{E}}{\partial \theta^2} + 2ik \frac{\partial \mathcal{E}}{\partial z} = 0.$$

LIST OF REFERENCES

- M. A. BANDRES and J. C. Gutiérrez-Vega, “Ince-Gaussian modes of the paraxial wave equation and stable resonators”, *Journal of the Optical Society of America A*, Volume 21, Number 5, pp. 873-880, May 2004.
- V. BARILON, “Special Functions” in C. E. Pearson, Ed., *Handbook of Applied Mathematics*, Van Nostrand Reinhold, New York, 1983.
- J. BLAU, W. B. Colson, B. W. Williams, S. P. Niles, and R. P. Mansfield, “Optical mode distortion in a short Rayleigh length free electron laser”, *Proceedings, 26th International Free Electron Laser Conference*, Trieste, Italy, 2004.
- W. B. COLSON, “Free Electron Laser Theory”, Ph.D. Dissertation, Stanford University, September, 1977.
- W. B. COLSON in W. B. Colson, C. Pellegrini, A. Renieri, Eds., *Laser Handbook, Vol. 6*, North Holland, Amsterdam, 1990.
- W. B. COLSON, J. Blau, G. Allgaier, S. Miller, T. Fontana, E. Mitchell, B. Williams, P. P. Crooker, “Multimode simulations of a short-Rayleigh length FEL”, *Proceedings, 25th International Free Electron Laser Conference*, Tsukuba, Japan, 2003.
- M. FRIGO and S. G. Johnson, “FFTW: An Adaptive Software Architecture for the FFT”, *Proceedings, 1998 International Conference on Acoustics and Signal Processing*, p. 1381, 1998.
- J. D. JACKSON, *Classical Electrodynamics*, Wiley, New Jersey, 1999.
- J. M. J. MADEY, “Stimulated emission of brehmsstrahlung in a periodic magnetic field”, *Journal of Applied Physics*, Volume 42, Number 5, pp. 1906-1913, April 1971.
- F. L. PEDROTTI and L. S. Pedrotti, *Introduction to Optics, Second Edition*, Prentice Hall, New Jersey, 1993.
- M. W. SAFNETT, “Propagation of multimode laser beams - the M^2 factor”, in D. R. Hall and P. E. Jackson, *The Physics and Technology of Laser Resonators*, IOP, Bristol, England, 1989.
- A. E. SIEGMAN, *Lasers*, University Science Books, Sausalito, 1986.
- A. E. SIEGMAN, “Defining, measuring, and optimizing laser beam quality”, *Proceedings: Laser resonators and coherent optics: Modeling, technology, and applications* (SPIE Conference), Los Angeles, CA, Jan. 18-20, (A93-53003 23-36) p. 2-12, 1993
- P. SPRANGLE, A. Ting, C. M. Tang, “Analysis of radiation focusing and steering in the free-electron laser by use of a source-dependent expansion technique”, *Physical Review A*, Volume 36, Number 6, pp. 2773-2781
- P. SPRANGLE, J. R. Peñano and B. Hafizi, “Propagation of Intense Short Laser Pulses in the Atmosphere”, *Phys. Rev. E*, 66, 046418, 2002.
- P. SPRANGLE, J. R. Peñano, A. Ting, B. Hafizi, and D. F. Gordon, “Propagation of Short, High-Intensity Laser Pulses in Air”, *J. Dir. Energy* 1, 73, 2003.
- B. W. WILLIAMS, *Jefferson Lab Free Electron Laser 10 kW Upgrade - Lessons Learned*, Technical Report NPS-PH-05-001, Naval Postgraduate School, Monterey, May 2005.
- D. ZWILLINGER, Ed., *CRC Standard Mathematical Tables and Formulae, 31st Edition*, Chapman & Hall, New York, 2003.

THIS PAGE INTENTIONALLY LEFT BLANK

INITIAL DISTRIBUTION LIST

1. Defense Technical Information Center
8725 John J. Kingman Road, STE 0944
Fort Belvoir, VA 22060-6218
2. Dudley Knox Library, Code 013
Naval Postgraduate School
Monterey, CA 93943-5100